Clay Minerals, (2008) **43**, 281–315

Acid-sulphate hydrothermal alteration of andesitic tuffs and genesis of halloysite and alunite deposits in the Biga Peninsula, Turkey

Ö. I. ECE[1,2,*], P. A. SCHROEDER[2], M. J. SMILLEY[2] AND J. M. WAMPLER[3]

[1] *Istanbul Technical University, Faculty of Mines, Department of Geological Sciences, Mineralogy-Petrography Division, Maslak 34469 Istanbul, Turkey,* [2] *The University of Georgia, Department of Geology, Athens, GA 30602-2501, USA, and* [3] *Georgia Institute of Technology, School of Earth and Atmospheric Sciences, Atlanta, GA 30332, USA*

(*Received 23 January 2007; revised 24 July 2007*)

ABSTRACT: The Biga Peninsula of NW Turkey is host to six major halloysite deposits in the Gönen, Yenice and Balya districts. Mineralization took place in areas of Permian limestone blocks where the Triassic Karakaya Complex is in contact with early Miocene calc-alkaline volcanic rocks. Hypogene halloysite mineralization was controlled by the intersection of minor faults in the vicinity of clay deposits. During the Pleistocene, activity of the North Anatolian Fault (NAF) brought ascending geothermal solutions through the fault zones to the surface, which led to hydrothermal alteration and halloysite formation. N-MORB normalized element values for each halloysite deposit and the volcanic rocks suggest genetic links. Alunite and halloysite were formed in the Turplu area where upwelling hydrothermal waters contained major H_2S and SO_2 acids. Only halloysite mineralization occurred in outflow areas of the same fossil geothermal field.

Pyrite and alunite samples from the Turplu deposits have $\delta^{34}S$ values of 0.6−1.8‰ and 4.8−7.9‰, respectively, with values for gypsum of 3.1−3.5‰. The $\delta^{34}S$ values of pyrite suggest that local meteoric waters had partially mixed with the dominant fluid during the closure stage of fossil hydrothermal activities. The range of δD values of halloysite samples from Turplu is −58.4 to −68.6‰. The $\delta^{18}O$ values for halloysite are in the range 16.7−18.1‰. All halloysite deposits in the study areas are either overlying or adjacent to limestone blocks, and these provide excellent drainage for the discharging geothermal waters. Subsurface drainage systems in the karstic environment and the SO_2-bearing thermal waters indicate the importance of acidic waters and the continuous leaching of elements in forming relatively pure hydrated halloysite. A steam-heated dissolution-precipitation model is proposed for the occurrence of all halloysite and alunite deposits. Sulphur gases (H_2S-SO_2) of hypogene origin rose from deep in the fault zone to the surface where they encountered oxygenated groundwater at the water table. The occurrence of H_2SO_4 in this hydrothermal system enhanced the acidity of geothermal waters provoking advanced argillic alteration. Hypogene alunite deposits also have large P_2O_5 contents, suggesting a parent material with a magmatic origin deeper than the alkaline tuffs. Halloysite is a fast-forming metastable precursor to kaolinite.

KEYWORDS: calc-alkaline volcanism, acid-sulphate thermal waters, hydrothermal alteration, halloysite, alunite, sulphur isotopes, Turkey.

* E-mail: ece@itu.edu.tr
DOI: 10.1180/claymin.2008.043.2.10

Halloysite is found in hydrothermal and residual volcanic deposits, but is less common in sediment-hosted kaolins (Murray & Keller, 1993). It usually forms from the alteration of rhyolitic volcanic glass and feldspar phenocrysts by a combination of weathering, hydrothermal activity (Harvey & Murray, 1993) and putative microbial processes (Tazaki, 2005). During the progressive alteration from the parent silicic volcanic rocks, the alkali content decreases and the Al and H_2O contents increase causing halloysite to replace feldspar. Bailey (1989) reported that the structure of halloysite forms by rolling of the layers, with the tetrahedral sheet on the outside of the curve in order to minimize the misfit of the larger tetrahedral and smaller octahedral sheets. He also summarized the properties of kaolinite and halloysite, proposing that tetrahedral Al is essential for the formation of the latter. Solid-state transformation is the major mechanism in the conversion of halloysite to kaolinite (Jeong, 1998), rather than a dissolution-precipitation system. Recently, Joussein *et al*. (2005) provided a comprehensive review on halloysite mineralogy, crystal structure, genesis, occurrence and physicochemical properties.

Historically, Keller (1963) and Keller & Hanson (1968) were the first to recognize that halloysite formation could be influenced by the presence of sulphate in geothermal waters, such those in the San Luis Potosi geothermal field of Mexico. Keller *et al*. (1966) also described an occurrence of hydrated halloysite in Stanford, Kentucky, where the groundwater pH range was 3.0–3.7. Hydrous halloysite in Indiana and Kentucky was also formed from cold meteoric-water solutions with large amounts of Si and Al, where oxidation of pyrite produces significant acidity (pH = 1–2). Hydrous halloysite precipitating out of cooling acid-sulphate geothermal waters at surface temperatures in Zacatecas, Mexico, was noted by Keller & Hanson (1969). Sequential alteration of rhyolitic rocks to a precursor of hydrous halloysite was later noted by Keller *et al*. (1971) in a hot spring in Michoacan, Mexico which yields water containing H_2S-SO_2 at 45ºC and pH = 3.5–3.7. From these studies, it appears that hydrated halloysite forms in SO_2-containing acidic solutions in either hot or cold waters.

The occurrence of alunite-natroalunite solid solution series in intimate association with hydrated halloysite was studied in the sediments of Carlsbad Cavern and Lechuguilla caves of New Mexico, where cave-forming waters contain significant concentrations of sulphuric acid (Polyak & Güven, 1996). The sulphuric acid-bearing waters, when exposed to clay-rich sediments, converted the clay minerals and quartz to alunite/natroalunite and hydrated halloysite. Hill (1990) reported that hydrated halloysite occurs in Carlsbad Cavern and other caves in the Guadalupe Mountains of New Mexico as a waxy and variably coloured (blue, blue-green, white and lavender) clay, associated with montmorillonite and filling sponge-like pockets in the limestone. Hill (1987) used hydrated halloysite as one indicator for the formation of the Guadalupe caves by solutions rich in sulphuric acid. A hydrogen sulphide-producing horizon was found in the lowest level of the Fiume Vento cave, Italy (near the water table), while gypsum blocks and hydrated halloysite were found at higher levels (Hill, 1986). The genetic relationships of two cryptokarstic (covered karsts) halloysite deposits from the Entre Sambre et Meuse region in Belgium and the Perigord region in France were compared and it was documented that oxidation of pyrite from overlying lignite beds provides waters of low pH, which infiltrate downwards through the strata. It is at this point that the transformation of kaolinite to smectite occurs, with further transformation to halloysite found on the surface of decarbonatized limestone. An important factor in the mode of formation is the downwards percolation of groundwater (Perruchot *et al*., 1997).

This study was carried out within the Sakarya zone of the Pontides, NW Turkey (see figure 1A in Ece & Schroeder, 2007). Figure 1 (this study) and figure 1 (in Ece & Schroeder, 2007) show six major halloysite deposits located in the Biga Peninsula (Yenice-Gönen-Balya district), NW Turkey (Turplu, Kızıldam, Kırıklar, Taban, Soğucak and Ilıcaoba) (see also Uygun, 1999). Only Turplu has alunite mineralization. The Ilıcaoba and Soğucak deposits have been exhausted. The remaining deposits are currently being mined by the ceramics industry, where the halloysite is used in the formulation of glazes. Total reserves are currently estimated at 50,000 tonnes. Three of the six major halloysite quarries are located NE of Yenice town (Fig. 1). The purpose of this paper is to examine the geochronological, geochemical and mineralogical characteristics of the halloysite-forming environments in NW Turkey and present a genetic model for the timing and conditions of their formation.

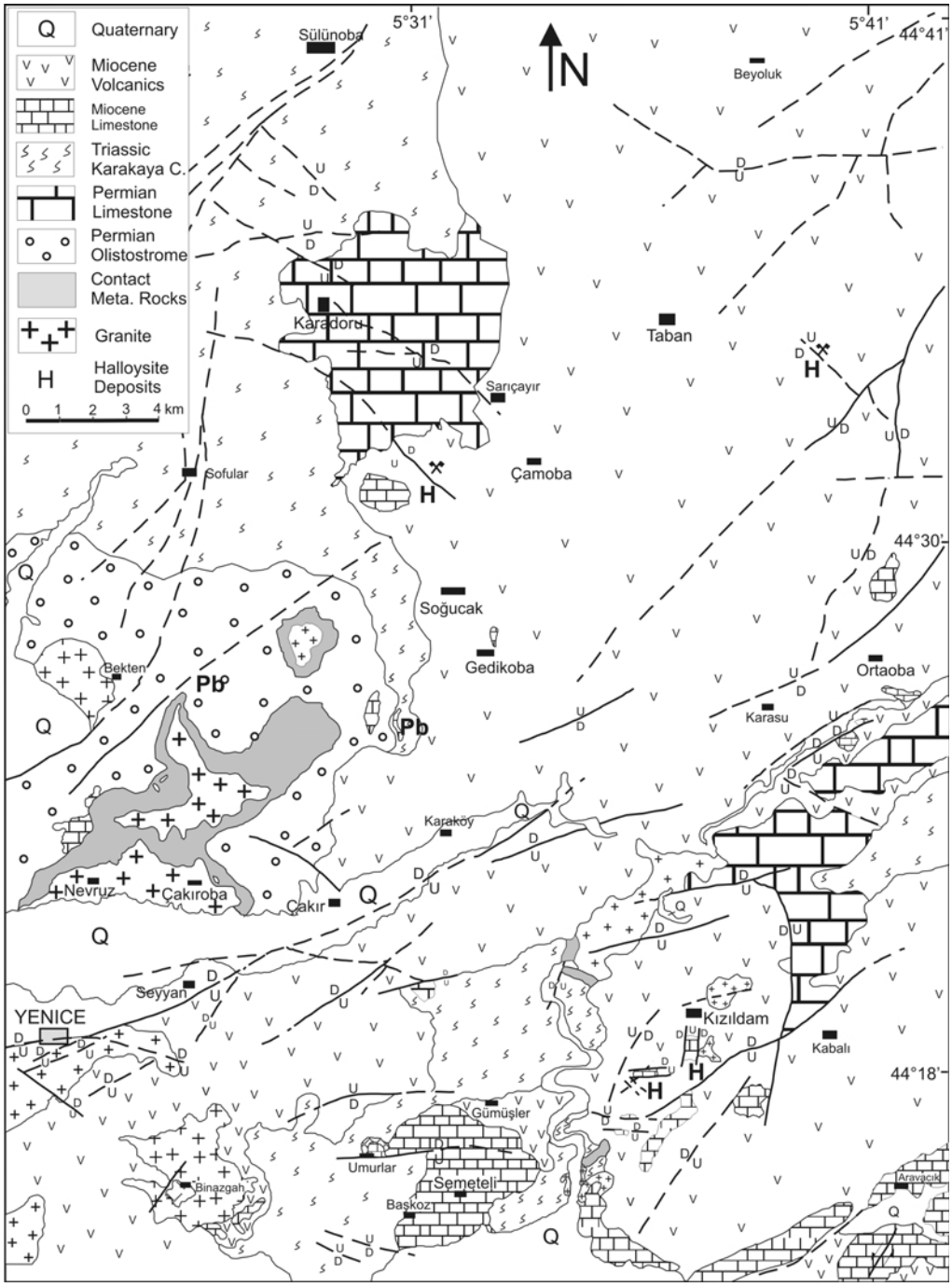

FIG. 1. Geological map of the study area showing the Kızıldam, Taban, and Soğucak quarries. Solid lines show the fault zone with relative displacement (U/D). The Yenice-Gönen main fault zone is currently active and last moved in 1953 (Mz = 7.2) (Herece, 1990; Gözler, 1984 and this work). Pb indicates the location of skarn-type Pb-Cu-Zn deposits. Kırıklar and Ilıcaoba quarries are located outside this map.

REGIONAL GEOLOGY

The regional geology of the study area has been reviewed by Ece & Schroeder (2007). In brief, a Permian limestone is the oldest known depositional unit near the clay deposits (Fig. 2). The limestone is associated with the Triassic Karakaya Complex, which consists of several tectonostratigraphic units. Four major units have been recognized in the Biga Peninsula, including (1) the Nilüfer Unit; (2) the Hodul Unit; (3) the Orhanlar Greywacke; and (4) the Çal Unit (Okay *et al*., 1991). The first two units are exposed in the study area. The Karakaya Complex mainly consists of low-grade metamorphic spilitic basalt with giant limestone blocks, calc-schists, mudstone, radiolarite, feldspathic sandstone, quartz-ite, conglomerate and siltstone. The lowest part of the Karakaya Complex (known as the Nilüfer Unit) is exposed to the NE of the town of Yenice and is made up largely of tuffs and volcanic rocks with intercalations of marble and phyllites. The Hodul Unit is exposed to the west of the Turplu halloysite deposit and to the north of the town of Yenice (Okay *et al*., 1991). The Karakaya Complex is overlain by the Jurassic–Cretaceous Bayırköy Formation, the Bilecik Limestone and the Vezirhan Formation. The subsequent early Miocene volcano-stratigraphic succession of the study area is summarized in Fig. 3. Along the Gönen-Yenice fault system, NW and SW of the town of Gönen, thermal waters have a temperature of 82ºC. In the Ekşidere region, NE of the study area, thermal waters have discharging temperatures of 42ºC.

Recent tectonic activity in Turkey is characterized by continental collision between the Eurasian and Arabian plates, which has led to continuous crustal thickening and shortening in eastern Anatolia. The Anatolian Block is moving west along the North Anatolian Fault (NAF) zone (Okay *et al*., 1999) which has caused a N–S extension due to the E–W compression (Okay *et al*., 2000). Early Miocene volcanics characterized by deposition of

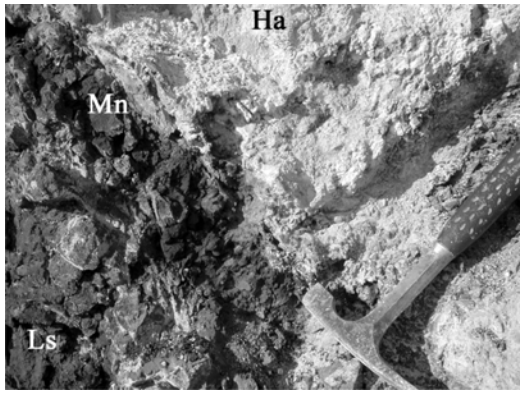

FIG. 2. Photograph of a limestone block (Ls) found 'floating' in a halloysite (Ha) matrix. The block is derived from the underlying Permian formation and was probably tectonically emplaced during post-Miocene volcanism. The dark Mn oxide-rich rim (Mn) shown here often coats limestone blocks and is attributed to pH-neutral conditions associated with limestone dissolution and also the mobilization of Mn and Fe associated with siderophores (Cornell & Schwertmann, 1996).

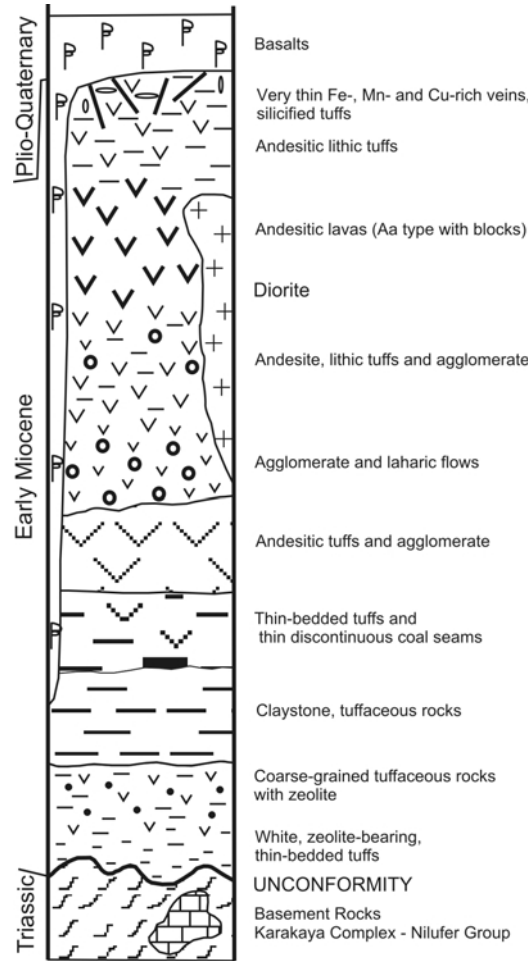

FIG. 3. Generalized volcano-stratigraphic section of the Ali Demirci, Turplu and Büyükpınar areas, east of the Yenice, Danışment and Balya areas.

calc-alkaline tuffs, ashes and pyroclastic rocks, have been modified in this extensional tectonic regime. Northeast–southwest *en echelon* faults constitute the western end segments of the NAF zone in the Biga Peninsula. Two phases of widespread volcanic activity are recognized (Fytikas *et al*., 1976). The first affected the North Aegean area from the Oligocene to mid-Miocene and the second started in the mid-Pliocene and continues to the present day. Between these two main phases, sporadic minor volcanism with a variable petrogenetic character is observed (Fytikas *et al*., 1984).

During the early Miocene wide areas were covered by andesites, dacites, rhyolites and acidic tuffs, with several large granodiorite plutons emplaced as shallow intrusions during this period (Siyako *et al*., 1989). This calc-alkaline volcanism largely ceased during the late Miocene. With the inception of the NAF in the late Miocene a large number of NE–SW trending dextral faults formed in the Biga Peninsula, all of which are still active today (Siyako *et al*., 1989; Okay *et al*., 1991). The Turplu halloysite and alunite deposits (south mine N39.7339º, E27.6735º; north mine N39.7412º, E27.6767º) are located in the southern part of Manyas-Danışment fault zone, to the north of Ali Demirci and to the west of Turplu. The Kızıldam deposit (N39.9206º, E27.4378º) and Taban deposit (N40.0528º, E27.4643º) are located west of the active Yenice-Gönen fault zone. Ilıcaoba (N40.02262º, E27.5501º) and Soğucak (N40.03753º, E27.3714º) quarries are located to the east and to the west of this main fault zone, respectively. Kırıklar quarry (N39.7505º, E27.2862º) is associated within another fault zone, which is sub-parallel to the Manyas-Danışment and Yenice-Gönen fault zones.

Yenice-Ilıca plutons

Granodiorite is exposed in many places to the north and south of the town of Yenice. K-Ar dating yielded ages of 18.8–21.9 Ma for the plutons (Table 1). Well exposed contact metamorphic aureoles 1–2 km wide (Fig. 1) indicate that the exposures are of a large pluton which cooled slowly. Slate, phyllite and discontinuous lens-shaped calc-schists are exposed along the contact zone of the pluton to the north of Yenice. Granodiorite plutons are exposed at Ilıca, Şamlı and Danışment, which are each located ~15 km from the Turplu deposit, to the north, northeast and northwest, respectively. In the vicinity of Karadağ, near Danışment, the mineralogical composition changes from granodiorite to fine-grained alkaline granite, with coarse-grained (3–4 cm) K-feldspars and minor mafic enclaves, which indicate the outer zone of the pluton. Fine-grained minerals are more altered, but coarse-grained crystals are more compact and relatively fresh. The joint fracture zones in Karadağ are planar ~30–60 cm wide, striking N50ºE and dipping 56ºNW. Major minerals of the plutonic rocks are plagioclase, K-feldspar, biotite, hornblende ± clinopyroxene ± opaque minerals. Secondary minerals epidote, sericite, chlorite and calcite formed due to alteration.

Small granodiorite plutons exposed in the Balya-Yenice-Gönen area can be interpreted as shallow-level intrusives, similar to the Evciler pluton described by Genç (1998). Here the plutonic rocks are medium-grained, grading into porphyritic and fine-textured rocks towards the marginal areas. The Yenice pluton clearly crosscuts the volcanic succession and generated a contact metamorphic aureole, suggesting that the granitic magma reached subvolcanic levels in the crust and crystallized under 0.5–1 kbar pressure (Öngen, 1978).

Halloysite deposits

Contact zones between limestone blocks and clays were exposed during mining operations in Kızıldam quarry. The original Permian limestone is micritic, thick-bedded and usually massive. Gypsum and anhydrite replacement on the surface of limestone blocks is common. Rare euhedral gibbsite flakes and alunite nodules (3–6 cm) were found next to limestone blocks in the Turplu halloysite quarry. The clays surrounding limestone blocks are generally smooth with slickensides and are thinly coated with a fine white and grey powder, sometimes waxy, heavily pigmented with purple to grey dendritic and Fe oxide-stained spotty moulding (Fig. 2).

Primary feldspar and biotite were completely replaced by smectite and illite in the overlying weathered volcanic rocks, which are locally accompanied by minor amounts of kaolinite and quartz. Smectite alteration grades into a distal zone characterized by an assemblage of illite, pyrite and amorphous Fe oxides. This distal alteration assemblage is associated with andesite lavas. In halloysite quarries, thin Fe- and Mn-rich bands surround the

TABLE 1. The results of K-Ar dating of granodiorite and andesite (G-6A and T-47) samples.

Sample	Material analysed	K (wt.%)	— Radiogenic Ar — (% of ^{40}Ar)	(pmol/g)	Apparent age (Ma)
G-1	Whole rock, pulverized	2.83±0.04	31	99±5	20.1±1.0
G-2	Biotite, chopped	7.00±0.11	74	264±6	21.6±0.6
G-2	Whole rock, pulverized	2.43±0.04	28	81±5	19.1±1.1
G-2	Whole rock, pulverized	2.43±0.04	27	78±4	18.4±1.1
G-3	Whole rock, pulverized	2.62±0.04	25	90±5	19.7±1.1
G-4	Biotite, chopped	7.01±0.11	84	266±5	21.7±0.5
G-4	Whole rock, pulverized	2.47±0.04	11	81±8	18.9±1.8
G-4	Coarser fraction of pulverized whole rock	1.49±0.02	14	48±6	18.4±2.2
G-5	Biotite, chopped	7.05±0.11	91	281±3	22.8±0.5
G-5	Whole rock, pulverized	2.44±0.04	23	83±5	19.5±1.2
G-6A	Whole rock, pulverized	2.95±0.04	51	95±3	18.4±0.7
G-6G	Biotite, chopped	5.41±0.08	77	226±5	23.9±0.6
G-6G	Whole rock, pulverized	3.25±0.05	46	117±4	20.7±0.8
G-7	Biotite, chopped	6.47±0.10	69	262±8	23.2±0.8
G-7	Whole rock, pulverized	3.15±0.05	48	122±4	22.3±0.8
G-7	Whole rock, pulverized	3.15	50	116±4	21.2±0.8
G-9	Biotite, chopped	6.55±0.10	86	268±5	23.4±0.6
G-9	Biotite, chopped, fine fraction	5.99±0.09	79	245±7	23.5±0.7
G-9	Whole rock, pulverized	2.63±0.04	25	97±4	21.2±1.0
G-10	Biotite, chopped	6.97±0.10	88	261±6	21.4±0.6
G-10	Whole rock, pulverized	3.22±0.05	18	105±7	18.8±1.3
G-10	Coarser fraction of pulverized whole rock	2.05±0.03	33	78±4	21.9±1.1
G-10	Finer fraction of pulverized whole rock	3.44±0.05	20	121±7	20.2±1.2
G-13	Biotite, chopped	7.28±0.22	67	295±10	23.2±1.1
G-13	Feldspar, chopped	9.13±0.14	76	352±8	22.1±0.6
T-47	Whole rock, pulverized	2.67±0.04	31	89±5	19.1±1.0
T-47	Whole rock, pulverized	2.65±0.04	47	91±5	19.7±1.1
North Quarry					
T-25	Alunite	7.43±0.11	26	8.5±0.3	0.66±0.03
T-28	Alunite	7.17±0.11	21	8.3±0.4	0.67±0.04
T-53	Alunite	7.97±0.12	33	10.7±0.4	0.77±0.03
T-55	Alunite	7.16±0.11	11	9.2±0.7	0.74±0.06
South Quarry					
T-102	Alunite	6.04±0.09	6	1.5±0.4	0.15±0.03
T-103	Alunite	6.01±0.09	5	1.1±0.3	0.11±0.03
T-106	Alunite	6.52±0.10	5	1.6±0.4	0.14±0.04
T-108	Alunite	6.91±0.10	3	0.7±0.3	0.06±0.03
T-119	Alunite	5.94±0.09	15	5.1±0.4	0.49±0.04
T-120	Alunite	7.51±0.11	14	4.6±0.3	0.36±0.03

Locations are as follows. G-1; Yeniköy-Çaypınar, east of Şamlı, G-2; Davutlar village, east of Şamlı, G-3; Fe-mine, dyke, west of Şamlı, G-4; east of Ilıca, G-5; west of Ilıca, G-6A; Kızıldam village, andesite, G-6G; Kızıldam, contact zone, G-7; Kocadere river, east of Kızıldam, G-9; Kocadere river bed, Kızıldam halloysite quarry, G-10; north of Yenice, G-13; Karadağ village, east of Danışment and T-47; Ali Demirci village, andesite.

large limestone blocks (Fig. 2), which suggests that these redox-sensitive metals in geothermal waters precipitated in neutral to basic conditions in micro-environments, perhaps facilitated by siderophore production (Cornell & Schwertmann, 1996). Gypsum bands and crystals were found on some limestone blocks, although this transformation did not continue for more than 0.2 m below the surface. Gibbsite-halloysite associations are present in limited abundance.

High-grade halloysite deposits are exposed at the Kızıldam and Taban quarries. The Taban and Turplu halloysite deposits display pyrite mineralization within fault clays, as well as realgar, cinnabar, orpiment, azurite and chalcopyrite mineralization, which is irregularly distributed as very small discontinuous bands in the clay body. Pyrite was often completely oxidized in the Kızıldam, Soğucak and Ilıcaoba halloysite deposits. In the Kırıklar quarry, limestone blocks are overlain by halloysite, although no limestone exposure is seen at the surface. In contrast, medium-bedded limestone formations are exposed in the vicinity of Ilıcaoba and Soğucak quarries, the latter in particular displays exfoliation textures of Fe oxide in cobble-sized altered tuffs, due to post mineralization effects of Fe migration from surface weathering along exfoliation planes.

Halloysite deposits were formed along the major fault zones and mineralization took place between the Permian limestone blocks within the Triassic Karakaya Complex and early Miocene calc-alkaline tuffs. Mineralization is located at the intersection of minor faults, with the halloysite deposits themselves ~10–20 m thick. Large carbonate blocks occur within clay deposits and are believed to have fallen into Miocene volcanic tuffs along the fracture zones by gravity mass-flow processes generated by regional tectonic uplift during the late Miocene (Okay *et al*., 1991; Harris *et al*., 1994). Local cryptokarstic terrains developed underneath and/or adjacent to the clay deposits. This undulating karstic bottom topography appears to result in a well drained subsurface lithology that accentuates the leaching of labile elements released by chemical weathering near the surface. The enhanced mobility of Ca, Na, Fe, Si and Mg in the meteoric geochemical environment leads to the enrichment of Al, which is manifest in the formation of halloysite deposits. Active tectonics and warm ascending geothermal waters which flushed over the parent tuffs led to leaching of certain elements. Vertical pH gradients resulted in the formation of halloysite and alunite above the karstic drainage systems.

The clay deposits are best exposed inside valleys along hill slopes, which are cut by small faults oriented quasi-perpendicular to rivers, such as the Kocadere River near Turplu. Representative samples of hydrated and dehydrated halloysites were collected from all deposits and alunite deposits were identified in hand specimens. Hydrated halloysite appears as lustrous pearly white to light yellowish to light pink nodules, while the dehydrated form under sunlight appears pasty or powdery and surrounded by small fractures. Alunite resembles white porcelain in hand specimen. It is harder than kaolin and less powdery than the nodules (Ece & Schroeder, 2007).

Turplu alunite deposit

Halloysite and alunite deposits located near Turplu occur along a strike-slip fault zone, ~20 km east of the town of Balya. This major fracture zone forms the boundary between Triassic metamorphic rocks to the west and Miocene andesitic volcanic rocks to the south and east of the Turplu halloysite deposits. There is also a minor skarn-type sulphate mineralization within the Permian carbonate rocks near these halloysite deposits.

Two halloysite deposits 1 km apart are present in the Turplu area, with the northerly deposit also containing abundant alunite. The base of the deposit is undulated due to the karstic bottom topography. The alunite distribution is controlled by the intersection of N50ºW and N60ºE fault zones. The southern deposit consists dominantly of hydrated halloysite, which resembles lustrous, white porcelain, light yellowish to light pink powdery nodules in hand specimen. Dehydrated specimens are reticulated by small fractures. The relatively impure material contains amorphous Fe oxides in various quantities. Within the clay body, exfoliated concentric textures of secondary Fe migration are common from core to rim in large cobbles, with the influence of supergene Fe remobilization from surface weathering obvious as a post-mineralization effect on the clay body.

The hydrothermal alteration zones are characterized by the destruction of all primary rock-forming minerals and the formation of alunite and halloysite in different horizons. Pyrite cubes 0.1–1 mm long

are commonly disseminated in the fault clays and occur as fine-grained aggregates, associated in places with chalcopyrite. In the alunite zone K-feldspar is completely replaced by bladed alunite, with alteration displaying a flower-shaped structure through the deep fault zone. Rare kaolinite occurs in the alunite zone in the interstices of intergrown alunite blades. Gibbsite-rich zones are detected between halloysite and limestone blocks in the lower part of the deposit. Alunite and halloysite ± rare kaolinite is observed in the outer alteration zone of the northern Turplu deposit (Ece & Schroeder, 2007).

The northern clay quarry is very rich in alunite with small deposits of halloysite in its central part. This field observation suggests that relatively high-temperature ascending geothermal waters came from the deep fault zone, spread around both sides of the fault zone and developed the funnel shaped alunite deposit, whereas halloysite formed in the upper part. Similar morphological occurences from Peru have been reported by Dill *et al*. (1997). The geothermal waters rose from numerous centres within the study area and several of them, as indicated by the form and distribution of the ore bodies, resemble the trunk of a tree from which the ore bodies at higher elevations branch and divide, commonly extending for a distance along fault planes.

The halloysite and alunite deposits are part of the largest hydrothermally altered area in the Balya-Yenice-Gönen district. To the south of Kocadere River at Turplu, step faults are sub-parallel to the river and display Mn-Fe-rich bands, which represent a multi-stage hydrothermal activity associated with the fracture system outside the clay deposits (figure 1 in Ece & Schroeder, 2007).

METHODS

Representative volcanic rock samples were collected from both fresh and altered exposures at the six quarry sites. The major elements were determined with a RIGAKU 3070 X-ray fluorescence (XRF) spectrometer according to Ece & Nakagawa (2003). Trace elements and rare-earth elements (*REE*) of all samples were determined by inductively coupled plasma optical emission spectrometry (ICP-OES) (Ece & Nakagawa, 2003). Mineralogical and geochemical data and techniques are detailed by Ece & Schroeder (2007). For sulphur isotope studies, SO_2 produced by heating gypsum, alunite and pyrite at 1050ºC was analysed using a Finnigan MAT252 gas-source mass spectrometer. The $\delta^{34}S$ values are reported relative to the primary standard, Canon Diablo Troilite (CDT). The accuracy is estimated to be ±0.2‰. The $\delta^{18}O$ and δD values for halloysite were measured at Southern Methodist University, Texas, USA, using standard fluorination lines (ClF3 or BrF5) and silicate extraction techniques. The K-Ar age values were determined at the Georgia Institute of Technology, USA. Whole-rock samples of andesite and granodiorite were pulverized and biotite and K-feldspar were separated and chopped in a blender till fine. This ensured equivalence of the respective portions taken for Ar and K measurements. The measurements were done using procedures such as those of Elliott *et al*. (1999). The amount and isotopic composition of the Ar were determined by mass spectrometry after isotope dilution with ^{38}Ar.

The K-Ar ages for alunite were obtained by a new method which varies from conventional K-Ar procedures in that the K content of each sample was determined from the solid residue remaining after Ar extraction, rather than from a separate sample. This procedure avoids error associated with weighing two discrete samples as well as sample heterogeneity in K and Ar contents. Small chips of alunite were used to avoid the possibility that crushing the material might introduce additional atmospheric Ar. In 1 h of heating at 300ºC, only minimal atmospheric Ar was released from the alunite samples. Most of the atmospheric Ar and all of the radiogenic Ar in these samples were released during heating at ~600ºC for 1 h. It is most likely that the Ar in alunite is released in association with the release of the hydroxyl water. Repeated heating of some samples at 600ºC showed no further Ar release, with no K lost from the samples at this temperature.

RESULTS

Geochemistry

The geochemical data for volcanic rocks and granodiorites are listed in table A1 of Ece & Schroeder (2007) and Table 2 (this study). A major element classification diagram for volcanic rocks indicates the seven analysed volcanic rocks are within, or very close to, the andesite field (Fig. 4a). Using the Nb/Y *vs*. Zr/TiO_2 diagram of Winchester & Floyd (1977), the volcanic rocks plot

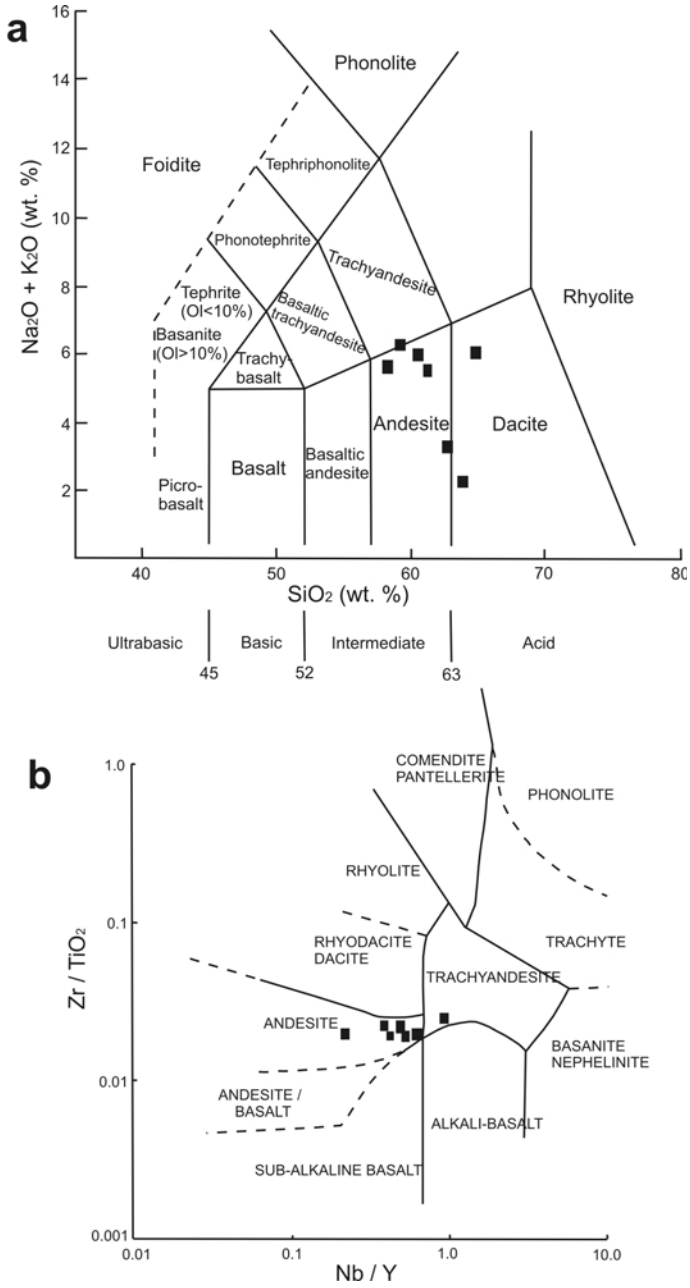

FIG. 4. (a) $Na_2O + K_2O$ *vs.* SiO_2 (Le Maitre, 1989) and (b) Zr/TiO_2 *vs.* Nb/Y plots of the volcanic rocks of the study area (Winchester & Floyd, 1977).

within the andesite and trachyandesite fields (Fig. 4b). The N-MORB normalized trace element and *REE* patterns of volcanic rocks (Fig. 5) compare favourably with magmas formed in a subduction-related volcanic setting similar to those observed in the calc-alkaline rocks of the central Andes (Thorpe *et al*., 1984; Harris *et al*., 1994). In particular, depletion of the highly incompatible elements Ti, Nb and Ta is indicative of such a setting. The large La (27.6–201.4 ppm), Ce

TABLE 2. Geochemical analyses (wt.%) of the granodiorites and andesites of the Yenice-Gönen-Balya area. N-MORB values are from Sun & McDonough (1989).

Sample no.	T-3	T-10	T-11	T-32	T-47	T-49	G-6A	G-1	G-2	G-3	G-4	G-5	G-6G	G-7	G-8	G-9	G-10	G-11	N-MORB
	Andesites						Granodiorites												
SiO_2	61.07	62.53	63.69	60.09	58.74	64.37	57.81	58.16	59.63	63.37	63.32	62.77	63.31	62.64	61.74	60.54	63.9	63.4	50.4
Al_2O_3	16.7	19.3	16.92	16.41	16.25	14.73	15.4	14.82	15.04	15.54	15.76	16.23	15.33	15.84	15.95	16.76	15.38	15.6	15.2
Fe_2O_3	5.18	2.43	5.31	5.54	6.04	5.12	5.53	5.25	4.82	4.71	4.87	5.04	4.83	5.07	5.64	4.96	4.63	4.92	9.44
MgO	1.89	0.07	0.56	2.16	2.51	1.99	3.6	3.45	2.56	2.38	2.39	2.4	2.4	2.41	2.35	2.7	2.1	2.27	8.96
CaO	4.68	0.1	0.05	5.27	5.44	4.3	3.89	5.75	5.27	2.15	4.92	5.09	4.53	4.56	4.37	4.79	4.38	4.36	11.4
Na_2O	3.15	0.15	0.2	3.23	3.22	2.94	2.3	2.58	2.78	3.25	3.36	3.39	3.11	3.31	3.31	3.58	3.37	3.39	2.3
K_2O	2.49	3.08	1.87	2.65	2.98	3.03	3.27	3.11	2.62	2.96	2.81	2.72	3.46	3.51	3.52	2.94	3.62	3.56	0.1445
TiO_2	0.65	0.95	0.74	0.65	0.63	0.52	0.72	0.68	0.58	0.56	0.53	0.54	0.59	0.63	0.62	0.72	0.6	0.56	1.267
P_2O_5	0.25	0.43	0.01	0.18	0.2	0.13	0.22	0.38	0.34	0.18	0.13	0.16	0.17	0.19	0.16	0.25	0.2	0.21	0.14
MnO	0.09	0.01	0.01	0.04	0.08	0.09	0.1	0.09	0.09	0.06	0.1	0.09	0.09	0.09	0.11	0.09	0.09	0.08	0.18
Cr_2O_3	0.004	0.003	0.002	0.005	0.002	0.002	0.005	0.024	0.009	0.002	0.002	0.001	0.001	0.002	0.002	0.002	0.001	0.001	–
H_2O	3.5		10.4	3	3.6	2	6.9	5.3	6	4.6	1.5	1.3	1.9	1.7	1.9	2.4	1.4	1.3	–
Ba	1564	1443	1240	1213	1338	1088	1045	1635	1302	1178	1102	1322	1057	1191	1077	1208	1054	1171	6.3
Sc	16	14	12	16	13	12	14	15	10	8	11	10	12	11	11	12	10	11	41.37
Mo	0.3	1.1	1	0.8	0.2	0.3	1	0.5	1.5	0.2	0.3	0.4	2.3	2	6.9	1.7	0.5	0.7	0.31
Cu	20.9	3.9	24	14.8	5.5	4.7	20.8	8.8	11.9	42.9	5.3	14	6.2	16.2	32.7	40.1	5.8	7.7	74.4
Pb	7.2	88.1	18.8	6.6	24.8	15.2	17.7	4.9	10.8	38.1	14.5	4.9	16.3	21.7	30.8	16.7	7.8	9.8	0.3
Zn	41	4	7	48	65	33	46	36	48	63	34	26	18	26	37	24	30	27	–
Ni	7.8	2	1.6	6.5	6.6	3.2	8.4	44.4	18.6	18.6	3.6	2.6	5.9	6.6	7.3	8.7	5.5	6.9	177
As	3.6	89.9	10.6	7.8	39.6	12.7	3.9	4.1	5.3	7.6	4.7	1.5	4	4.1	2.7	2.7	1.6	2.3	–
Cd	0.1	0.5	0.1	0.4	0.3	0.2	0.1	0.1	0.1	0.1	<0.1	0.1	<0.1	<0.1	0.2	0.1	<0.1	0.8	–
Sn	2	1	1	1	4	<1	2	3	2	2	2	1	3	1	2	2	2	2	1.1
Sb	0.8	0.4	0.4	0.6	10.1	0.7	0.2	0.1	<0.1	0.6	0.2	0.1	0.2	0.1	0.2	0.2	0.1	0.1	0.01
Bi	0.1	3.5	1.2	<0.1	0.3	<0.1	<0.1	0.1	0.3	0.1	0.2	<0.1	0.3	0.2	0.1	0.3	0.1	0.1	–
Tl	0.1	0.4	0.1	0.1	0.1	0.1	0.1	0.2	0.2	0.1	0.2	0.2	0.1	0.1	0.1	0.1	0.3	0.2	0.0014
Co	43.4	5.9	22.2	42.3	29.4	33.8	24.3	22.6	38	28.4	119.5	33	43.4	32.4	39.6	26.3	46.9	142.2	50
Cs	4.9	6	15.7	6.7	14.1	3.2	7.9	4.5	3.7	3.7	5.3	4.6	16.9	6	9.3	3.4	5.2	6.4	0.007
Ga	18.2	21.7	19.4	17.2	20	14.8	17.6	18.9	18.5	18.1	18.8	18.3	17.2	17.6	17.8	19.9	18.1	18.8	–
Hf	3.8	4.3	4.7	3.5	4.2	3.2	4.4	5.8	5.2	4.1	4.1	4.2	5.5	5.1	4.6	4.7	5	5.6	2.05
Nb	10.9	11.2	10.9	11.1	11.8	10.1	14	16.2	14.4	12.6	12.3	10.9	15.9	15	16	15.4	18.1	16.1	2.33
Rb	85.7	76.6	67.2	95	127	111.9	122.5	127.9	115.1	103.8	116.9	115.1	157.9	154.1	162.7	117.6	166.3	168.6	0.56
Sr	651.5	887.4	136.1	608.9	692.4	448.2	509.8	561.1	441	476.7	513.1	505.7	557.3	601.6	612.3	765.2	603.9	656.6	90
Ta	0.9	1.1	1.1	1.3	1	1.5	1.3	1.2	1.2	1.3	1.5	1.2	1.7	1.4	1.8	1.4	1.9	1.9	0.132
Th	19.9	19.4	11.7	19.8	21.6	19.9	30.3	26.9	23.4	21.9	29	25.1	40	40.1	37.8	30.1	35.7	31.2	0.12
U	5.4	24.9	5.7	6	6.3	5	8.9	6	7.4	3.9	5.8	7.4	13.5	10.8	11.8	8.5	9.6	9.8	0.047

V	158	152	154	145	130	96	136	125	100	90	112	112	104	108	109	141	107	118	262			
W	161.1	133.6	31.7	850.6	96.1	1223	51	67.2	176.6	92.5	761.1	197.5	258.1	173.5	261.4	158.4	293.6	833.1	0.01			
Zr	128.1	156.1	156.5	127.6	144.8	113	146	209.6	174	148	136.4	133.4	176.2	174.3	160.7	159.1	166	184.7	74			
Y	25.4	14.1	9.1	20.7	29.6	20.1	21.8	22.7	22.1	13.7	22.7	20	25	25	27.4	24.1	28.4	25.2	28			
La	46.3	201.4	27.6	42.5	50.9	36.5	45.1	46.4	41.2	40	47.8	32.9	55.1	55.7	61.2	35	66.4	74.5	2.5			
Ce	75.8	335.8	39.6	69.9	76.9	59.9	79.3	85.9	74.2	69.9	77.9	58	97.1	100	110	62.8	113.5	118.3	7.5			
Pr	8.16	31.34	3.5	7.47	8.73	6.29	8.05	9.87	8.14	7.19	7.77	6.04	10.33	10.18	11.55	6.59	11.67	11.41	1.32			
Nd	32.4	95.1	11.5	27.4	34.9	23.5	31.3	40.2	33.2	26	27.6	22.7	40.2	39.3	44.7	26.7	44.5	42.8	7.3			
Sm	5.8	13	2.1	5	6	3.9	5.5	7.1	6.5	4.4	4.8	4.4	6.8	6.9	8.1	5.1	7.7	7.4	2.63			
Eu	1.48	2.8	0.38	1.25	1.43	0.97	1.35	1.39	1.21	1	1.17	1.07	1.34	1.41	1.56	1.55	1.57	1.47	1.02			
Gd	5.6	6.62	1.61	4.3	5.26	3.69	4.46	4.94	4.66	3.25	4.2	3.9	5.11	5.2	6.25	4.77	6.01	5.66	3.68			
Tb	0.75	0.85	0.26	0.62	0.76	0.55	0.62	0.69	0.66	0.5	0.63	0.55	0.76	0.75	0.82	0.66	0.85	0.79	0.67			
Dy	4.24	3.99	1.54	3.39	4.35	3.29	3.71	3.67	3.62	2.63	3.56	3.16	4	4.02	4.62	3.98	4.73	4.28	4.55			
Ho	0.87	0.56	0.33	0.68	0.95	0.62	0.72	0.7	0.7	0.46	0.74	0.66	0.81	0.8	0.89	0.75	0.89	0.8	1.01			
Er	2.42	1.41	1.07	1.95	2.85	1.9	2.18	2.04	2.12	1.33	2.12	2.06	2.39	2.39	2.57	2.24	2.63	2.39	2.97			
Tm	0.35	0.26	0.19	0.3	0.39	0.28	0.32	0.29	0.29	0.19	0.32	0.29	0.34	0.34	0.39	0.32	0.4	0.36	0.456			
Yb	2.17	1.8	1.33	1.95	2.61	1.85	2.25	1.82	2.09	1.3	2.22	2.02	2.37	2.27	2.62	2.19	2.79	2.36	3.05			
Lu	0.37	0.3	0.25	0.3	0.44	0.33	0.34	0.3	0.34	0.21	0.34	0.32	0.39	0.38	0.39	0.34	0.42	0.39	0.455			

(39.6−335.8 ppm), Th (11.7−30.3 ppm) and Pb (6.6−88.1 ppm) contents of the samples are also consistent with a post-collisional hybrid origin (Pearce *et al*., 1990; Harris *et al*., 1986). Geochemical studies suggest that there is a significant shallow-level intrusion of crustal material into the mantle-derived magma (Karacık & Yılmaz, 1998). The enrichment of Ba and U (Fig. 5) is further evidence of significant assimilation of crustal material by the mantle-derived magma.

N-MORB normalized values for the granodiorites (Fig. 5) reveal that there is no genetically significant difference in the chemical composition of the andesites and the granodiorites. Major and trace element (including *REE*) compositions of halloysite samples from five major halloysite quarries are listed in Table 3. N-MORB normalized values for the *REE* in the halloysites (Fig. 6) are much more variable than those for the igneous rocks and are distinctly smaller in the samples that have been almost completely altered to halloysite (as indicated by loss on ignition >20%, Table 3). They are generally consistent with the idea that the halloysites were derived from the enclosing volcanic rocks, although the completely altered Kiriklar samples are distinctly depleted in light *REE*.

Electron microprobe analysis (EMPA)

Average, minimum and maximum values of the elements analysed using an electron microprobe (EMP) are listed in Table 4. The results show significant chemical variations between alunite crystals within the same thin section and samples from the north and south quarries. Apatite (or francolite) in the hexagonal ($P6_3m$) system has a structural site that accepts many substitutions $(Ca,Sr,Pb,REE,Na,Ba)_5(PO_4,AsO_4,CO_3,SO_4)_3(OH,F,Cl)$. Alunite, in the trigonal ($R3m$, $R\bar{3}m$) system has a crystal structure that also allows for a broad range of isomorphous substitution $(K,Na,Ca,Fe^{3+},NH_4,Ba,Pb,Cu)Al_3(SO_4)_2(OH)_6$. The open-site mixing and substitution potential for both alunite and apatite structures are equally high. Therefore, the observed trace element and *REE* contents of alunite (figure A4 in Ece & Schroeder, 2007) and apatite record similar precipitation conditions (Table 4). Phosphate-rich grains in the alunite matrix appear as bright areas in back-scattered electron scanning electron microscope (BSE-SEM) images (Fig. 7). These sand-sized bright areas, when magnified, display smaller

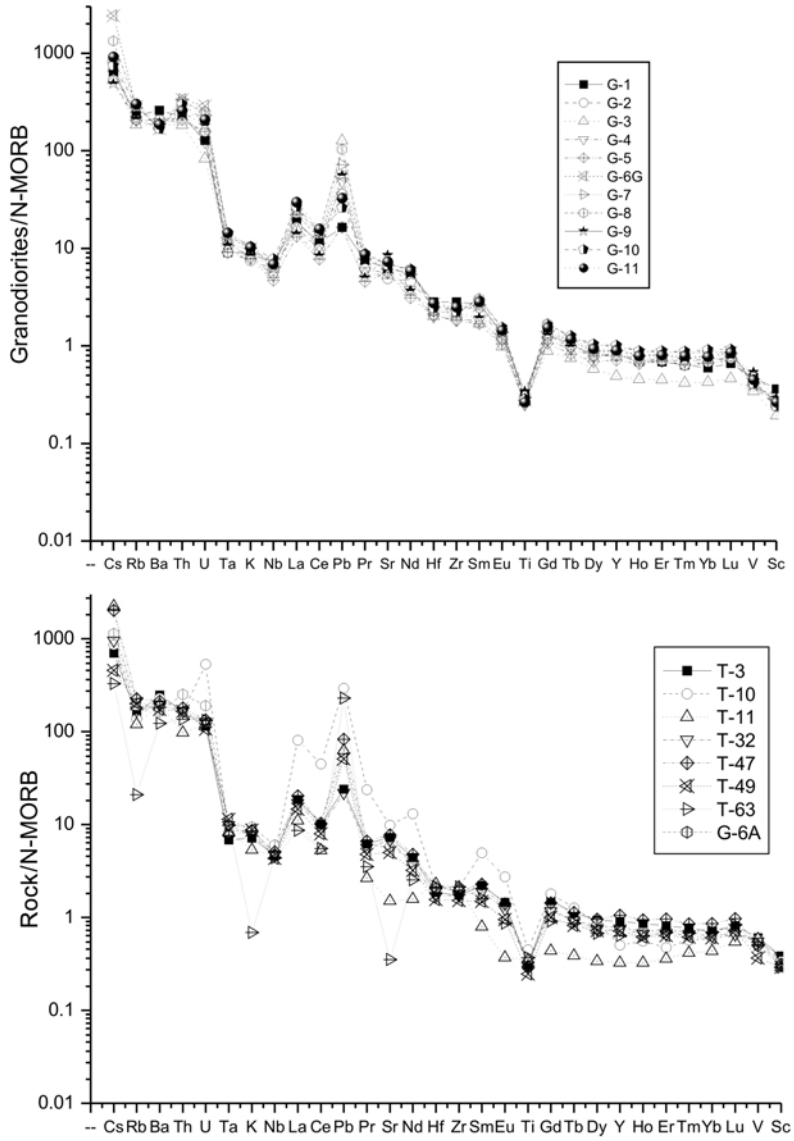

FIG. 5. N-MORB-normalized element abundance patterns for granodiorites (G-samples) and andesites (T-samples) from the study area. N-MORB normalizing ratios are from Sun & McDonough (1989).

bright and dark grains: the bright grains indicate enrichment in Ca-phosphate (Table 4). In contrast, the dark grains inside the sand-sized bright areas appear to be alunite. These are rich in sulphate and low in phosphate, with a heterogeneous phosphate distribution like that of alunite. Alunite nodules and cobbles from the south quarry generally have more P_2O_5, K_2O and Na_2O in their matrix, while north quarry samples have more SiO_2, SO_4 and less P_2O_5 in their matrix. The relationship between Ca and P does have a constant pattern even in different areas of the same samples (Table 4). No discrete phosphate is detected and phosphate contents range from 0.56 to 2.0 wt.% in the crystal structure of alunite. However, this value is ~0.75 wt.% in alunites containing maximum K_2O.

TABLE 3. Major (wt.%), trace and *REE* (ppm) analyses of halloysite samples. KK = Kırıklar, KZ = Kızıldam, S = Soğucak, TB = Taban and I = Ilıcaoba deposits.

Sample no.	KK-1	KK-2	KK-7	KK-10	KK-16	KK-19	KK-24	KK-25	KK-26	KK-27	KK-29	KZ-1	KZ-4	KZ-11	KZ-12	KZ-13	KZ-14
SiO_2	54.68	54.98	34.18	69.94	51.79	39.68	39.96	62.09	38.76	41.66	39.26	42.43	43.42	42.04	46.2	41.43	72.33
Al_2O_3	16.45	17.51	38.95	16.84	21.17	34.49	34.14	21.09	33.88	31.79	34.41	34.32	32.39	30.45	31.33	32.42	15.8
Fe_2O_3	6.69	5.63	0.39	2.85	7.66	0.21	0.63	2.59	0.57	1.38	0.09	0.14	0.77	4.57	1.13	1.95	2.4
MgO	4.42	1.96	0.03	0.19	0.35	0.01	0.01	0.54	0.01	0.13	0.06	0.03	0.08	0.13	0.26	0.03	0.24
CaO	7.06	5.16	0.03	0.29	0.06	0.02	0.01	0.15	0.02	0.03	0.05	0.09	0.1	0.06	0.09	0.04	0.08
Na_2O	2.82	2.49	0.03	1.64	0.36	0.04	0.02	1.9	0.03	0.01	0.02	0.04	0.03	0.03	0.04	0.02	0.35
K_2O	1.91	2.29	0.02	1.48	0.88	0.02	0.02	1.78	0.02	0.02	0.02	0.02	0.02	0.02	0.02	0.02	3.75
TiO_2	0.7	0.73	0.02	0.51	0.63	0.01	0.01	0.59	0.01	0.11	0.02	0.03	0.09	0.59	0.36	0.11	0.69
P_2O_5	0.26	0.26	0.25	0.02	0.15	0.58	0.16	0.08	0.45	0.46	0.52	0.12	0.14	0.12	0.08	0.11	0.17
MnO	0.1	0.1	0.01	0.01	0.01	0.01	0.01	0.01	0.01	0.01	0.01	0.01	0.01	0.01	0.01	0.01	0.01
Cr_2O_3	0.01	0.011	0.001	0.001	0.002	0.002	0.001	0.008	0.002	0.578	0.02	0.003	0.002	0.006	0.004	0.004	0.002
LOI	4.6	8.6	26	6.2	16.7	24.9	25	9	26.2	23.7	25.5	22.6	22.6	21.7	20.1	23.7	3.8
Ba	1364	805	12	221	283	74	10	445	44	71	14	163.2	12.9	35.8	38.6	38.9	2395
Sc	15	24	1	8	18	1	1	13	1	6	1	6	10	12	9	4	8
Mo	0.1	0.1	1.3	0.8	39.9	0.1	0.4	0.3	0.1	0.4	0.1	0.1	0.4	0.1	0.1	0.1	30.8
Cu	36.5	22.3	5.7	6.5	13.6	9.1	7	119.4	17.3	12.9	5.6	47.1	23.2	33.7	36.4	38.7	9.7
Pb	13.6	7.4	1.5	8.1	49.1	1.4	3.3	32	1.6	22.1	0.7	7.3	60.2	1.8	0.7	3.6	49.5
Zn	46	74	46	1	481	7	14	274	22	33	9	16	5	16	11	10	2
Ni	8.6	7.9	269.6	8.3	52	35.3	86.4	10.5	65.1	75.7	47.8	94.5	14	108.3	104.2	76.2	0.5
As	1.8	3.1	11	4.4	58.4	2	58.8	88.2	3.7	6.5	4.7	354.2	1213.6	611.5	126.1	108.8	7.4
Cd	0.1	0.1	0.4	0.1	180.6	0.2	0.4	1	0.1	0.4	0.1	0.2	0.1	0.1	0.1	0.3	0.1
Sb	0.2	0.1	0.4	0.1	0.1	0.1	0.4	0.6	0.1	0.2	0.1	2.6	9.7	4.4	3.3	0.9	0.2
Bi	0.1	0.1	0.1	1.7	2.4	0.1	0.1	0.1	0.1	0.4	0.2	0.1	0.1	1.1	1.2	1.1	2.2
Ag	0.1	0.1	0.1	0.1	0.1	0.1	0.1	0.1	0.1	0.1	0.1	0.1	0.1	0.1	0.1	0.1	0.1
Au	0.5	17.8	1.2	0.8	2.2	0.5	0.5	1.1	0.5	4.8	2.7	1	2	3	2	1.6	2.8
Hg	0.01	0.01	0.01	0.01	0.01	0.01	0.01	0.01	0.01	0.01	0.01	0.02	0.03	0.01	0.01	0.01	0.01
Tl	0.1	0.1	0.1	0.1	0.1	0.1	0.1	0.2	0.1	0.1	0.1	0.3	0.2	0.1	0.1	0.1	0.4
Co	36	20.3	19.6	22.3	213.7	15.7	49.3	46.2	34.9	33.7	20.9	20.7	29.3	16.8	42.4	22.6	13.7
Cs	2	7.8	2.2	11.4	5.7	0.4	1	18.3	0.5	8.1	2	1.5	1	0.6	1.1	1	0.9
Ga	18.4	19.1	0.5	18.3	19.1	0.5	0.5	20.2	0.5	7.5	2.1	1.6	2.4	13.5	9.8	6.5	16.1
Hf	4.3	4.7	0.5	4.4	3.6	0.5	0.5	3.7	0.5	1	0.5	0.5	0.5	2.9	2	0.5	5.2
Nb	13	7.4	0.5	14.6	5.7	0.5	0.5	7.3	0.5	1.9	0.5	0.5	1	8.3	5.6	0.5	17.4
Rb	57.8	109.6	2.1	108	37.9	0.5	0.7	102.7	0.5	2.5	0.8	1.2	0.7	0.5	0.5	0.8	141.8
Sn	2	1	1	2	1	1	1	2	1	1	1	1	1	1	1	1	11
Sr	864	380.4	2.7	257.1	221.8	0.5	4.1	230.2	1.1	2.8	5.3	7.6	5.3	7.3	8.7	5.6	311.1
Ta	1.2	0.6	0.1	1.3	0.4	0.1	0.1	0.6	0.1	0.1	0.1	0.1	0.1	0.5	0.4	0.1	1.4
Th	33.3	13.3	0.2	20	8.8	0.3	0.7	9.9	1	3.7	0.4	0.3	1.5	5.8	2.6	1.4	17.9
U	4.1	4.1	0.6	3.7	1.7	1.2	0.3	3.5	0.5	1	0.7	2.3	3.7	7.1	5.4	2.5	3.8
V	124	163	82	77	99	47	98	119	35	182	29	23	70	177	67	36	117

TABLE 3. (*contd.*)

Sample no.	KK-1	KK-2	KK-7	KK-10	KK-16	KK-19	KK-24	KK-25	KK-26	KK-27	KK-29	KZ-1	KZ-4	KZ-11	KZ-12	KZ-13	KZ-14
W	40.2	16.3	3.4	60.6	53.7	3.2	5.7	36.8	2.2	14.9	5.3	12.8	51.9	28.2	112.8	6.5	165.5
Zr	154.2	147.9	4.1	135	127.1	0.5	0.5	135.5	0.9	27.6	4	5.8	20	112.4	69.5	14.5	179.7
Y	25.3	32.8	12.1	46	22.6	10.8	1.7	34.1	20	19.5	2.5	0.5	1.5	2.3	2.4	1.3	16.9
La	62.8	40.8	1.9	75.1	25.2	0.6	0.5	14.5	0.5	1.1	1	0.5	4.7	1.4	1	0.8	36.4
Ce	112.3	70.9	5.6	131.3	48.5	2.3	0.9	28.5	2.8	3.2	1.5	0.5	7.6	2.6	2.8	1.5	68.1
Pr	11.88	8.32	0.92	16.3	5.52	0.73	0.14	3.17	0.97	0.7	0.23	0.11	0.85	0.33	0.37	0.22	7.04
Nd	46.6	35.3	6.5	62.8	25.5	7.4	1.4	15.5	10.3	7.2	2	0.4	2.3	1.6	1.6	1.1	27
Sm	7.7	7.1	3.4	10.3	6.9	5	0.9	3.4	8.3	6	1.7	0.1	0.4	0.3	0.4	0.2	3.8
Eu	1.63	1.66	1.16	2.14	1.94	1.72	0.23	0.94	2.84	2.03	0.59	0.05	0.11	0.07	0.1	0.05	0.79
Gd	5.65	6.31	4.85	7.85	6.54	6.06	0.89	4.21	9.86	6.9	1.78	0.15	0.31	0.34	0.37	0.19	3.29
Tb	0.75	0.93	0.74	1.22	0.95	1.11	0.14	0.67	1.81	1.26	0.34	0.02	0.06	0.05	0.06	0.04	0.48
Dy	4.16	5.19	4.57	7.61	5.29	6	0.79	4.27	9.97	7	1.59	0.12	0.32	0.3	0.38	0.18	2.83
Ho	0.8	1.04	0.74	1.51	0.87	0.9	0.11	0.91	1.51	1.09	0.23	0.05	0.06	0.07	0.08	0.05	0.54
Er	2.35	2.82	1.77	4.63	2.45	2.14	0.27	2.95	3.71	2.69	0.55	0.05	0.15	0.24	0.23	0.12	1.63
Tm	0.33	0.46	0.24	0.71	0.36	0.3	0.05	0.43	0.54	0.41	0.06	0.05	0.05	0.05	0.05	0.05	0.25
Yb	2.32	2.78	1.48	4.7	2.28	2.05	0.16	2.87	2.98	2.28	0.45	0.05	0.21	0.25	0.25	0.18	1.57
Lu	0.37	0.47	0.16	0.79	0.32	0.16	0.02	0.46	0.3	0.25	0.04	0.01	0.04	0.11	0.05	0.02	0.27

Table 3 (*extended*)

Sample no.	S-1	S-3	S-6	S-10	S-11	S-Mn	TB-1	TB-2	TB-6	TB-7	TB-8	TB-9	I-2	I-10	I-12	I-16	I-18	I-19	I-21
SiO_2	41.16	41.98	56.18	39.61	42.71	33.65	72.12	39.8	41.19	40.7	8.25	38.56	69.27	41.28	43.92	39.6	57.97	37.68	40.21
Al_2O_3	35.41	36.49	21.63	33.08	36.53	23.64	17.15	34.38	35.48	34.95	7.8	34.58	18.61	35.54	34.09	35.08	19.89	37.5	34.96
Fe_2O_3	0.11	0.31	4.82	1.64	0.15	25.07	0.5	0.48	0.3	0.39	62.39	0.59	0.33	0.11	0.11	0.09	6.85	0.11	0.06
MgO	0.02	0.02	0.68	0.12	0.08	0.07	0.96	0.17	0.06	0.1	0.95	0.34	0.79	0.12	0.07	0.05	1.01	0.17	0.03
CaO	0.01	0.08	0.32	0.05	0.01	0.02	0.08	0.05	0.01	0.01	0.09	0.12	0.06	0.04	0.02	0.04	0.13	0.07	0.06
Na_2O	0.01	0.03	0.05	0.02	0.02	0.02	0.17	0.05	0.02	0.03	0.01	0.06	0.1	0.03	0.05	0.04	0.08	0.03	0.05
K_2O	0.02	0.02	0.83	0.02	0.02	0.02	4.88	0.05	0.02	0.02	0.02	0.05	4.69	0.12	0.33	0.02	4.46	0.26	0.02
TiO_2	0.01	0.12	3.04	0.01	0.31	0.19	0.6	0.02	0.01	0.01	0.09	0.04	0.72	0.03	0.06	0.01	0.82	0.04	0.01
P_2O_5	0.01	0.24	0.51	0.17	0.01	0.11	0.06	0.03	0.18	0.26	0.2	0.01	0.01	0.04	0.07	0.09	0.15	0.09	0.07
MnO	0.01	0.01	0.01	0.01	0.01	0.001	0.01	0.01	0.01	0.01	3.11	0.01	0.01	0.01	0.01	0.01	0.01	0.01	0.01
Cr_2O_3	0.001	0.007	0.05	0.035	0.006	0.006	0.002	0.001	0.001	0.002	0.001	0.001	0.001	0.001	0.001	0.005	0.001	0.001	0.001
LOI	23.2	20.6	11.7	25.2	20.1	16.9	3.3	24.8	22.7	23.5	16.5	25.4	5.1	22.6	21.2	24.9	8.3	23.9	24.4
Ba	33	121	104	33	10	10	743	262	21	21	54	229	1120	43	64	19	1788	71	44
Sc	9	36	32	19	5	21	8	1	1	1	2	1	12	2	3	1	13	3	1

Mo	0.2	0.2	0.6	0.2	0.1	2.1	1.4	2.7	5	4.8	71.2	0.2	0.5	0.1	0.4	1	2.1	1	0.2
Cu	20.3	9.2	50.5	8.4	4.5	35.6	0.9	29.3	7	3.5	27.6	55.3	4	2.7	12.3	7.4	4.1	7.4	5.6
Pb	7.3	0.1	62.7	1	0.2	4.4	10.6	31.1	34.8	297.1	339.5	315.8	43.8	12.7	115.6	77	16.9	77	46
Zn	23	6	8	3	11	1136	2	47	9	17	2087	697	6	246	60	171	29	171	476
Ni	65.2	33.1	52.5	6.6	27.6	187.2	0.4	178.9	9.8	9.3	104.3	283.5	1.1	99.8	165.3	121.7	4.7	121.7	248.7
As	2.2	2.8	107.2	4.4	0.5	31	3.6	12	4.2	3.2	22.2	7.4	21.3	2.3	1.9	2.6	19	2.6	7.4
Cd	0.1	0.1	0.1	0.1	0.1	0.1	0.1	0.1	0.1	0.1	1	0.1	0.3	0.1	0.8	0.6	0.2	0.6	1.1
Sb	0.1	0.1	2.9	0.1	0.1	2.4	0.1	0.1	0.1	0.1	4.2	0.1	4.2	2	3.7	5	0.9	5	0.9
Bi	0.1	0.1	37.3	0.1	0.1	2	1.3	0.4	1.3	3.4	15.5	12.7	1.1	0.5	0.5	0.3	0.7	0.3	0.2
Ag	0.1	0.1	0.1	0.1	0.1	0.1	0.1	0.1	0.1	0.1	0.1	0.1	0.1	0.1	0.1	0.3	0.1	0.3	0.1
Au	0.5	2.5	1.9	1.5	0.8	0.7	0.9	0.5	0.5	0.5	0.5	0.5	21.5	3.2	3.3	0.6	3.3	0.6	0.5
Hg	0.01	0.01	0.01	0.01	0.01	0.01	0.01	0.001	0.01	0.03	0.01	0.01	0.1	0.08	0.03	0.06	0.03	0.06	0.02
Tl	0.1	0.1	0.2	0.1	0.1	0.1	0.3	0.1	0.1	0.1	0.9	0.2	0.4	0.3	0.1	0.4	0.8	0.4	0.5
Co	37.5	15.2	10	27.4	51.3	113.5	22.4	33	10.7	18	580	60.5	32.3	14	36.1	13.2	27.8	30.1	21.7
Cs	0.3	1.3	5.1	0.2	1	0.9	4.7	1.6	0.5	0.7	0.7	2.9	29.1	17	8.3	12.5	29.8	18.9	14.6
Ga	0.7	1.6	20.2	0.8	11.5	6.5	18.2	0.7	0.5	0.5	8.8	2.5	20.4	0.7	1.8	0.5	19.4	1.4	0.5
Hf	0.5	0.5	6.4	0.5	1.7	1.1	4.4	0.5	0.5	0.5	0.5	0.5	5.2	0.5	0.5	0.5	4	0.5	0.5
Nb	0.5	2.5	48.7	0.5	6.9	4.6	14.4	0.5	0.5	0.5	1.2	0.5	19	0.8	1	0.5	11.1	0.9	0.5
Rb	0.7	1.5	47.9	0.5	0.9	1.5	222.7	1.8	0.5	0.6	1.3	4.4	292.3	10.2	25.8	3.2	291.6	20.3	4.2
Sn	1	1	8	1	3	1	3	1	1	1	4	1	2	1	1	1	1	1	1
Sr	1.1	416.7	110.4	111.2	1.1	1	49.9	17.7	1.4	5.8	12.6	19	31.8	12.1	11.3	13.3	227.6	13.8	43
Ta	0.1	0.2	3	0.1	0.5	0.4	1.4	0.1	0.1	0.1	0.1	0.1	2.8	0.1	0.1	0.1	0.8	0.1	0.1
Th	0.2	0.6	8.4	0.2	1.1	6.5	19.7	0.7	0.1	0.1	5.5	1.7	8	0.4	1.4	0.1	20.4	1.4	0.1
U	0.3	0.7	7.2	0.3	0.6	1.3	5.8	0.7	2.6	1.9	23.5	1.8	5.3	0.6	0.6	0.4	7.3	0.7	0.5
V	5	94	288	82	9	210	100	61	90	73	109	32	137	42	64	37	174	79	39
W	2.7	4.7	10.2	12.1	52.6	40.7	162.2	0.8	2.1	5.2	31.7	9.2	662.7	18.8	17.7	10.8	77.4	39.8	3.4
Zr	4.7	15.6	235.9	2.2	56.6	36	159.3	6.6	1.3	1.6	15.1	4.5	156.2	11.2	11	1.3	145.8	14.6	1.2
Y	3.6	36.4	41	8	6.5	78.6	10.5	0.5	0.4	0.5	99.2	7.6	5.2	7.2	1.7	5.4	19.1	9.3	6.1
La	2	58	77.5	11.7	4.7	3.3	49.6	5.2	0.6	1.5	17.6	1.9	28.1	1.2	4.5	0.5	75.3	2.2	0.5
Ce	5.9	124.8	150.7	23.9	7.8	7	90.5	6.2	1.4	3	45.9	3.4	51.2	2.1	8.1	0.8	135	3.9	0.5
Pr	0.34	14.95	17.88	2.82	1.03	1.31	9.08	0.39	0.15	0.43	4.63	0.87	4.75	0.22	0.89	0.03	15.57	0.4	0.02
Nd	1.4	57.1	76.6	10.7	4.7	7.4	32.8	1.2	0.8	2	24.5	4.5	16.4	1	3.8	0.4	60.3	1.6	0.4
Sm	0.3	10.7	19.4	2.7	0.9	2.7	4.7	0.3	0.3	0.4	8.1	1.4	2.3	0.2	0.7	0.1	9.5	0.5	0.1
Eu	0.08	2.38	6.01	0.57	0.16	0.9	1.01	0.06	0.12	0.19	2.61	0.42	0.37	0.13	0.18	0.08	1.84	0.25	0.05
Gd	0.51	11.48	28.52	2.9	0.76	6.21	2.91	0.26	0.43	0.57	12.74	1.58	1.15	0.68	0.59	0.39	5.85	1.33	0.24
Tb	0.1	1.93	4.41	0.44	0.15	1.49	0.35	0.02	0.07	0.07	2.36	0.24	0.17	0.12	0.08	0.1	0.68	0.23	0.07
Dy	0.64	10.25	19.71	2.33	1	12.56	1.86	0.09	0.28	0.53	14.41	1.14	0.87	0.7	0.48	0.55	3.49	1.64	0.62
Ho	0.14	1.62	2.45	0.38	0.23	2.75	0.37	0.05	0.06	0.07	2.9	0.25	0.16	0.2	0.06	0.15	0.67	0.35	0.14
Er	0.43	3.49	4.87	0.78	0.71	7.84	1.17	0.05	0.1	0.15	8.18	0.63	0.45	0.56	0.16	0.45	1.82	0.82	0.44
Tm	0.05	0.48	0.54	0.08	0.12	1.2	0.19	0.05	0.05	0.05	1.25	0.08	0.08	0.06	0.05	0.06	0.29	0.15	0.06
Yb	0.3	2.62	3.14	0.39	0.7	7.26	1.44	0.06	0.06	0.14	7.67	0.61	0.66	0.5	0.19	0.4	2.18	0.99	0.4
Lu	0.07	0.32	0.41	0.05	0.13	0.97	0.23	0.02	0.02	0.02	1.13	0.1	0.12	0.08	0.03	0.06	0.35	0.16	0.06

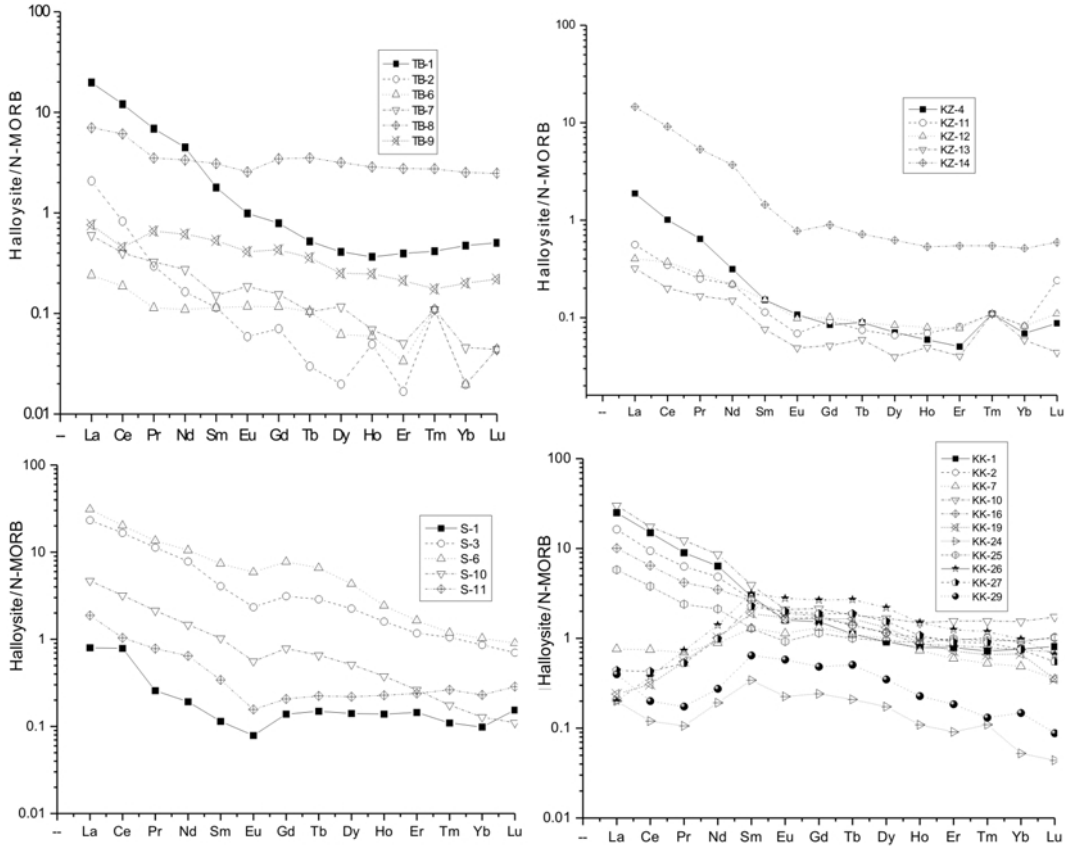

FIG. 6. N-MORB-normalized element abundance patterns for major halloysite deposits. N-MORB normalizing ratios are from Sun & McDonough (1989). TB = Taban, KZ = Kızıldam, S = Soğucak and KK = Kırıklar quarries.

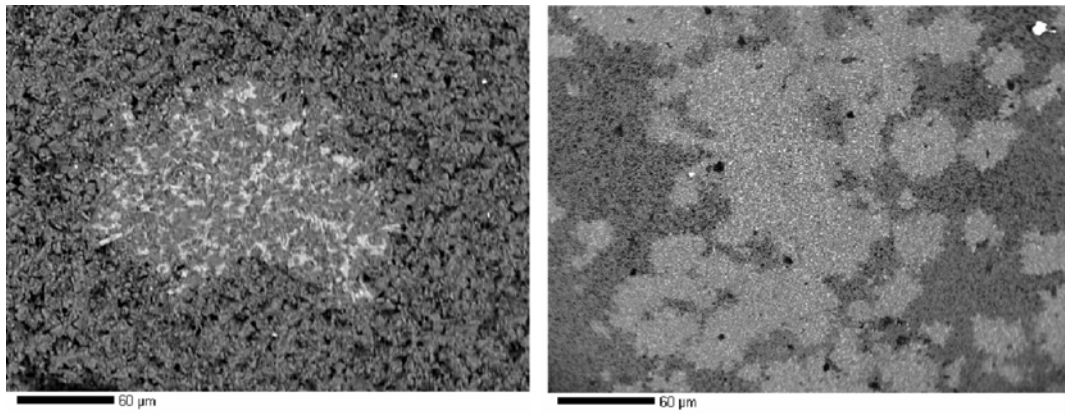

FIG. 7. BSE-SEM images of alunite sample T-55. Dark areas are alunite-rich matrix and bright areas are phosphate-rich grains. Bright points inside the bright grains are almost pure phosphate crystals and dark points are phosphate-poor alunites.

TABLE 4. EMPA (wt.%) of the alunite matrix and phosphate-rich grains found in the matrix. The average values of analyses are written under each element with the number of analyses shown in parentheses. Samples T-55, T-55A, T-28 and T-25 are from the north mine and T-109 is from the south mine.

Sample no.	T-55			T-55A			T-28	T-25	T-109
		Bright areas			Bright areas				
	Matrix Min – Max	Bright grains Min – Max	Dark grains Min – Max	Matrix Min – Max	Bright grains Min – Max	Dark grains Min – Max	Matrix Min – Max	Matrix Min – Max	Matrix Min – Max
SiO_2	0.09–0.2	0.0–0.073	0.01–0.04	0.08–0.32	0.0–0.01	0.048–0.053	0.006–0.21	0.76–2.61	0.0–0.16
	0.18 (5)	0.03 (3)	0.03 (3)	0.17 (4)	0.005 (2)	0.05 (2)	0.09 (3)	1.19 (8)	0.07 (9)
Al_2O_3	28.82–37.83	4.39–12.12	36.71–44.62	33.66–36.45	0.29–2.24	39.34–45.89	26.35–49.36	28.42–48.74	30.4–40.13
	32.93 (5)	9.35 (3)	39.73 (3)	35.0 (4)	1.26 (2)	42.62 (2)	41.63 (3)	39.07 (8)	37.10 (9)
K_2O	3.05–4.93	0.77–1.01	1.50–1.79	3.94–6.57	0.25–0.71	1.66–1.93	1.85–2.66	1.84–6.25	2.52–5.22
	4.12 (5)	0.85 (3)	1.66 (3)	5.14 (4)	0.48 (2)	1.80 (2)	2.38 (3)	3.97 (8)	3.26 (9)
Na_2O	0.53–0.83	0.21–0.4	0.28–0.72	0.37–0.88	0.14–0.46	0.11–0.56	0.24–0.60	0.08–0.62	0.12–0.44
	0.63 (5)	0.28 (3)	0.42 (3)	0.62 (4)	0.31 (2)	0.33 (2)	0.37 (3)	0.31 (8)	0.25 (9)
SO_4	17.42–23.45	2.22–5.58	18.59–26.59	17.66–20.94	0.34–1.28	20.78–25.34	24.16–25.7	16.55–26.11	15.83–21.98
	20.37 (5)	3.83 (3)	23.28 (3)	19.66 (4)	0.81 (2)	23.06 (2)	24.71 (3)	20.56 (8)	19.13 (9)
P_2O_5	0.96–2.65	22.96–33.85	0.41–2.99	0.47–1.70	35.91–37.97	0.46–1.73	0.54–0.85	0.28–0.77	1.95–3.44
	1.63 (5)	27.53 (3)	1.89 (3)	1.13 (4)	36.94 (2)	1.10 (2)	0.74 (3)	0.53 (8)	2.90 (9)
Fe_2O_3	0.0–1.04	0.0–1.04	0.0–0.85	0.4–0.74	0.05–0.7	0.0–0.5	0.0–0.05	0.0–0.72	0.0–0.68
	0.53 (5)	0.43 (3)	0.53 (3)	0.58 (4)	0.37 (2)	0.25 (2)	0.002 (3)	0.42 (8)	0.26 (9)
MgO	0.0–0.008	0.0–0.04	0.0–0.5	0.02–0.03	0.0–0.0	0.0–0.015	0.0–0.04	0.0 –0.066	0.0–0.026
	0.002 (5)	0.014 (3)	0.02 (3)	0.03 (4)	0.0 (2)	0.008 (2)	0.015 (3)	0.03 (8)	0.007 (9)
CaO	0.71–1.63	31.64–49.72	0.67–2.48	0.51–1.18	52.04–56.99	0.79 –1.32	0.17–0.41	0.05–0.4	0.58–1.61
	1.07 (5)	40.0 (3)	1.65 (3)	0.85 (4)	54.52 (2)	1.06 (2)	0.31 (3)	0.27 (8)	0.98 (9)

$(OH)_6$ theoretical weight loss 24.6%

TABLE 5. $\delta^{34}S$ values from alunite, halloysite and skarn-type Pb-Zn-Cu mineralization in the study area.

Sample ID	$\delta^{34}S$	North Quarry	South Quarry	Skarn	Kızıldam Quarry
T-25	6.93	Alunite			
T-28	5.72	Alunite			
T-28A	5.82	Alunite			
T-38	0.98	Pyrite			
T-43	5.95	Alunite			
T-45	5.03	Alunite			
T-90	7.56	Alunite			
T-90A	7.88	Alunite			
T-95	5.24	Alunite			
T-95	5.32	Alunite			
T-96	5.12	Alunite			
T-53	5.55	Alunite			
T-53	6.14	Alunite			
T-55	5.86	Alunite			
T-116	4.79	Alunite			
T-120	7.06	Alunite			
T-99	1.78			Pyrite	
T-100	1.97			Pyrite	
T-101	2.11			Pyrite	
T-121	2.71			Pyrite	
T-122	2.58			Pyrite	
T-123	2.68			Pyrite	
T-63	1.02		Pyrite		
T-80	1.19		Pyrite		
T-81	0.53		Pyrite		
T-82	1.77		Pyrite		
T-84A	1.47		Pyrite		
T-84	1.38		Pyrite		
T-85	0.62		Pyrite		
T-94	1.54		Pyrite		
T-102	4.55		Alunite		
T-103	4.72		Alunite		
T-104	5.50		Alunite		
T-105	6.78		Alunite		
T-106	3.80		Alunite		
T-106	3.80		Alunite		
T-107A	3.19		Alunite		
T-107	4.40		Alunite		
T-108	4.62		Alunite		
T-109	7.20		Alunite		
T-115	4.11		Alunite		
T-119	6.87		Alunite		
G-1	3.52		Gypsum		
G-2	3.49		Gypsum		
G-3	3.05		Gypsum		
G-9	0.37				Pyrite
G-9	0.71				Pyrite

K-Ar geochronology

K-Ar dating of biotite extracted from the granitoid intrusives gives age values in the range 21.4±0.6 Ma to 23.9±0.6 Ma (Table 1). Since emplacement was at a shallow level, the rock may have cooled quickly through the Ar-closure temperature for biotite, in which case these age values indicate that the related granitoid intrusions

took place over a short time period extending from very late in the Oligocene to early in the Miocene. K-Ar age values for whole-rock samples are consistently lower than those for corresponding biotites, probably because of continued loss of radiogenic Ar from feldspar during cooling after the closure temperature for biotite had been reached. An alternative interpretation is that the biotites contain some excess radiogenic Ar, but that seems unlikely in view of (1) the consistency of the age differences between biotite and whole rock; and (2) the differences between the conditions of formation of the shallow intrusives of this study and the typical rocks (from metamorphic terranes and major fault zones) where excess Ar has been found in biotite. K-Ar age values for andesite whole-rock samples (G-6A and T-47) are consistent with their formation early in the Miocene.

K-Ar age values for four alunite samples from the Turplu north quarry calculated using the new method are all within 0.1 Ma of 0.7 Ma (Table 1). Their near concordance suggests that the alunite formation here occurred during a short period of time. Age values for four of six alunite samples from the south quarry are 0.1 Ma (±0.1 Ma), suggesting much more recent formation of the majority of the alunite in this area.

Stable isotope data

The sulphur isotope analytical data were collected from the Turplu quarries, adjacent skarn sulphides just west of the Kocadere River and pyrite crystals in the granodiorite adjacent to the Kızıldam deposit (Table 5). In Turplu the $\delta^{34}S$ values range from +4.8 to +7.9‰ for alunite, +0.6 to +1.8‰ for pyrite from the south halloysite quarry (there are larger values (1.8−2.7‰) for pyrite from the skarn) and +3.1 to +3.5‰ for gypsum.

The range of δD values of halloysite samples from Turplu is −58.4 to −68.6‰ (Table 6). The paired $\delta^{18}O$ values for halloysite range from 16.7 to 18.1‰ (Table 6). Figure 8 shows a plot of the δD and $\delta^{18}O$ values for Turplu halloysite samples. There is no published O isotopic fractionation factor between water and halloysite, because there are fewer isotopic studies of halloysite than of kaolinite (Sheppard & Gilg, 1996). Both minerals have the same ideal stoichiometric composition; however halloysite contains additional interlayer water. We expect that halloysite samples were dehydrated before the isotopic analyses, thus exchangeable water was not a factor. We used the kaolinite-water O isotopic fractionation factor proposed by Sheppard & Gilg (1996):

$$1000\ln\alpha_{\text{kaolinite}-\text{water}} = 2.76 \times 10^6 \times T^{-2} - 6.75$$

The kaolinite line in Fig. 8 corresponds to kaolinite in equilibrium with meteoric waters at 20ºC (calculated using the fractionation equations of Sheppard & Gilg, 1996; temperature in K). The line labelled S/H is equivalent to kaolinite in equilibrium with meteoric waters at a temperature of ~35ºC. Sheppard & Gilg (1996) reported slightly smaller H- and O-isotope fractionation factors for halloysite than for kaolinite. Ziegler *et al*. (2003) estimated an average shift of ~3‰ (up to 5‰) and modified the kaolinite-water fractionation equation accordingly to:

$$1000\ln\alpha_{\text{halloysite}-\text{water}} = 2.76 \times 10^6 \times T^{-2} - 9.75 \quad (T \text{ in K})$$

The halloysite line of Fig. 8, on or near which the Turplu data fall, was calculated assuming meteoric waters at 20ºC.

DISCUSSION

In the study area, extensive hydrothermal activity developed in the vicinity of crosscutting fault zones, thereby creating intensive alteration patterns and enhancing the differential mobility of large amounts of major and trace elements as they pass through the karstic limestone. The source of Al and Si for the formation of halloysite was the parent andesitic tuffs underlying the andesitic lavas. Aluminium is essentially immobile in such environments, but Si is partially mobile. Thus, we propose the following

TABLE 6. O and H isotopic composition of pure halloysite samples from the Turplu deposit. T-87 and T-12 are from the south and T-56 and T-27 from the north quarries.

Sample no.	H_2O (wt.%)	δD (‰)	$\delta^{18}O$ (‰)
T-87A	12.52	−67.7	16.9
T-87B	12.24	−68.6	17.3
T-12	12.91	−64.9	18.1
T-56	13.46	−66.4	16.7
T-27A	13.13	−58.4	16.9
T-27B	13.02	−59.3	17.0

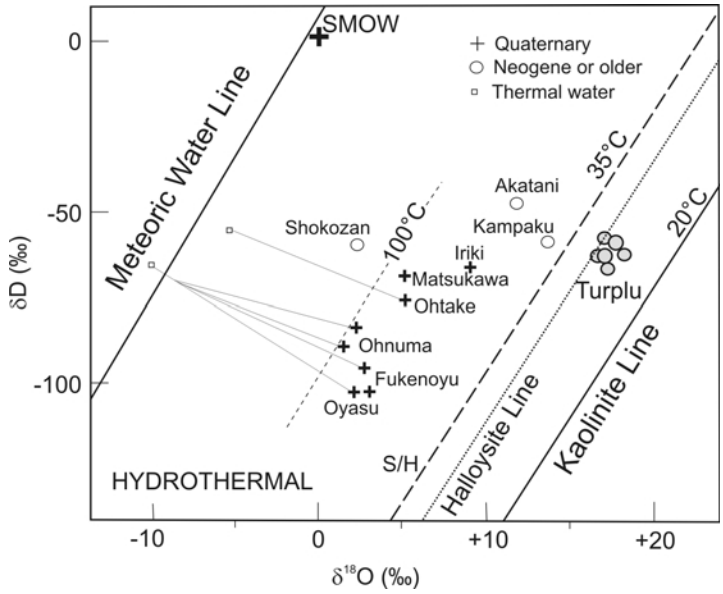

FIG. 8. The δD and $\delta^{18}O$ values of halloysites from the Turplu mine, hydrothermal kaolinites from active geothermal fields and thermal waters near kaolinite localities in Japan (Hayba *et al*., 1985). The meteoric water line is $\delta D = 6.8\delta^{18}O + 10.5$ (Harris *et al*., 1999). The light dashed line shows the δD-$\delta^{18}O$ relation of kaolinite in equilibrium with meteoric water at 100ºC. Supergene *vs.* hypogene lines are taken from Sheppard & Gilg (1996). The area to the left of the S/H line indicates a hypogene origin, with the right-hand side indicating supergene origin due to weathering effects on isotope exchange after clay mineralization.

alteration models for the formation of halloysite and alunite-halloysite. In both models, dissolution-precipitation mechanisms were proposed to explain how andesitic tuffs dissolved, converted to an Al-hydroxide gel and crystallized as halloysite and alunite.

Sulphur isotope data

The smaller $\delta^{34}S$ values of pyrite suggest that local meteoric water had partially mixed with geothermal fluids during the closing stages of fossil hydrothermal activity. Pyrite in fault clays appears to have formed at relatively neutral pH conditions. According to Rye *et al*. (1992), the $\delta^{34}S$ distribution of alunites in hydrothermal environments can be classified as follows; (1) magmatic hydrothermal origin (+9/+27‰); (2) supergene (−1.9/+12‰); (3) steam-heated (+4.1/+7.6‰); and (4) magmatic steam (−3.9/+2.7‰). In magmatic hydrothermal systems the isotopically light sulphur ($\delta^{34}S \approx 0$) in sulphides is derived from H_2S, whereas the isotopically heavy sulphur ($\delta^{34}S > 10$) in alunite is derived from H_2SO_4. The enriched $\delta^{34}S$ composition of the alunite suggests that the source of the sulphate had the isotopic composition of bulk magmatic sulphur (Rye *et al*., 1992). The source could have been SO_2 or H_2S that was oxidized by groundwater interaction in a steam-heated environment (Love *et al*., 1998). We assume that such a steam-heated model is more applicable to this study. This is further supported by phosphate inclusions in alunite samples, associated with deep leaching of phosphate minerals by hydrothermal fluids.

Sulphur is more susceptible to mobilization than the *REE* and most trace elements, and granitoid-associated hydrothermal ore deposits have $\delta^{34}S$ values of −10 to +15‰ (Ohmoto & Goldhaber, 1997; Poulson *et al*., 1991; Ishihara *et al*., 2000). The isotopic compositional difference indicates that the chemistry of the sulphur source varied between alunite and pyrite episodes in Turplu deposits. Another explanation is that the geochemical solutions had the same $\delta^{34}S_{H_2S}$ value, but that the pH of the fluid increased during the formation of pyrite (Ohmoto, 1972), which occurred during the latest stage of hydrothermal activity.

Physicochemical conditions of sulphur-bearing fluids

Palaeo-hydrology features of the study area are similar to that of groundwaters presently migrating through most of the Biga Peninsula, using the Permian limestone as a carrier bed (Yalçın, 1997). This is supported by studies in the Kazdağı massif recharge area and Turplu-Gönen-Eksidere geothermal fields, which are located ~100 km to the east (Yalçın, 1997). Reduced SO_4^{2-} in geothermal waters of the outflow areas relative to upflow areas in north Turplu alunite deposits, may explain the rarity of hypogene alunite nodules in the south Turplu halloysite deposit. A high sulphur fugacity caused alunite precipitation in north Turplu alunite deposit. The lack of sulphate minerals in fault-zone clays where pyrites are present and the positive $\delta^{34}S$ values of those pyrites suggest that the sulphur-bearing fluids during the late stages of hydrothermal activity had acidic pH and low f_{O_2} (Ohmoto, 1972) values. The mole fraction of SO_2 (>400ºC) or SO_4^{2-} (<400ºC) (Ohmoto & Rye, 1979) in hydrothermal fluids was sufficiently low so that the sulphide species (e.g. H_2S) prevailed during the deposition of sulphide minerals. The lack of pyrite minerals in the north Turplu alunite body strongly indicates that the f_{O_2} was adequately high to maintain SO_4^{2-} as the dominant sulphur species relative to $H_2S_{(aq)}$ during alunite deposition. The removal of an enormous quantity of oxidized H_2S (as pyrite along the fault zones of Turplu deposits) from the fluid phase ($SO_4^{2-}{}_{(aq)}$) probably further increased the SO_4^{2-} to $H_2S_{(aq)}$ ratio in the fluids (Ohmoto & Rye, 1979) during late-stage pyritization. Thermodynamic-based calculations suggest SO_2-rich solutions are the most likely degassing products of relatively oxidized magmas (Brimhall & Ghiorso, 1983; Whitney, 1984). Sulphur dioxide gas disproportionates to H_2S and H_2SO_4 below 400ºC in the presence of water by the following reactions (Holland, 1965, 1967; Sakai & Matsubaya, 1977): $SO_2 + H_2O = H_2SO_3^{2-}$ and $4H_2SO_3^{2-} = 3H_2SO_4 + H_2S$, depending on sulphur redox conditions. Using this approach, the interaction of the sulphuric acid solutions with the andesitic tuffs may explain the origin of halloysite and the alteration zones in the Biga Peninsula, as well as the formation of pyrite.

Thermodynamic constraints suggest that $\log f_{O_2} = -42$ is the boundary between H_2S and HSO_4^- and above this line, alunite is stable at pH <3 and pyrite is stable below the slightly inclining line for all pH <7 (figure 11 in Cunningham *et al*., 1998). For the formation of alunite, $\log f_{O_2}$ of the deep fluids was -42 at pH <3 in an oxidising environment, with $\log f_{O_2} > -42$ at pH 3–6 for the formation of halloysite. Oxygen fugacity *vs*. pH studies show that pervasive Fe oxides, kaolinite and a lack of pyrite are consistent with condensation of volatiles and mixing with shallow, steam-heated waters, resulting in oxidation of H_2S, a decrease in the pH and reaction of the fluids with the permeable wall rock (Cunningham *et al*., 1998). Al_2O_3-SiO_2-H_2O stability diagrams indicate that halloysite and imogolite are unstable with respect to kaolinite (Kittrick, 1969; Su & Harsh, 1994; Jeong, 1998). The difference in Gibbs free energy values of kaolinite (−3799.4 kJ/mol) and halloysite (−3780.7 kJ/mol) at 25ºC favours the transformation of halloysite to kaolinite. Based on kinetic considerations, halloysite is a fast-forming metastable precursor to kaolinite.

Hydrogen and oxygen isotope data

Figure 8 shows the δD and $\delta^{18}O$ compositions of Turplu halloysite samples and a group of kaolinites from active hydrothermal fields in Japan. Hayba *et al*. (1985) noted that the isotopic composition of kaolinites formed in a steam-heated environment plot very close to the line representing kaolinites in equilibrium with meteoric waters at 100ºC.

All Turplu halloysite samples fall around the halloysite-water line in Fig. 8. The kaolinite line corresponds to kaolinite in equilibrium with meteoric waters at 20ºC (calculated using the fractionation equations of Sheppard & Gilg, 1996) and the S/H line is equivalent to kaolinite in equilibrium with meteoric waters at temperatures of ~35ºC. Figure 8 also clearly shows that halloysite δD and $\delta^{18}O$ values can be distinguished according to their supergene or hypogene origin. This result corresponds with other sulphur isotope studies which indicate a similar hypogene origin. However, the fossil hydrothermal systems responsible for clay alteration were to be evolved by meteoric water during the post-mineralization period and consequently isotopic equilibrium reflects a lower temperature, resulting in halloysites relatively enriched O. The enrichment in $\delta^{18}O$ explains why the values of halloysites from fossil geothermal fields are shifted to the right, close to the kaolinite line, whereas δD and $\delta^{18}O$ compositions of kaolinites from the current active

geothermal fields of Japan are close to the 100ºC kaolinite line (Fig. 8). It should be emphasized that some isotopic exchange may not be complete and differential exchange should be taken into consideration (Sheppard & Gilg, 1996). Using similar approaches, the isotopic compositions of whole-rock, feldspar and quartz samples from hydrothermal deposits of the Marysvale volcanic field in Utah reveal $\delta^{18}O$ values in the range 0.2−4.7‰ for whole rock, −3.7−7.5‰ for feldspar phenocrysts and 1.5−11.4‰ for quartz, with a trend of $\delta^{18}O$ values which become systematically enriched towards the surface (Cunningham *et al*., 1998).

Supergene vs. hypogene

The genetic distinction between alunite and aluminium-phosphate-sulphate (APS) minerals containing hypogene and supergene kaolinization can be further examined on the basis of geochemical approaches using plots of Zr *vs*. TiO_2, Cr+Nb *vs*. Ti+Fe and Ba+Sr *vs*. Ce+Y+La (Dill *et al*., 1997; Dill, 2001). The enrichment of S, Ba and Sr is common in kaolin formed during hydrothermal alteration, whereas Cr, Nb, Ti and La are mainly concentrated during weathering (Dill *et al*., 1997). A similar situation is seen in Peruvian kaolin deposits where central zones of the Andean mountains also have calc-alkaline volcanism. This is similar to the hybrid origin of post-collision calc-alkaline volcanism in the study area of this work. Dill *et al*. (1997) found that hypogene kaolin deposits in Peru are enriched in S and P due to the presence of alunite and assumed that the source of P is in phosphate-bearing minerals, which appear during the later stages of magma differentiation. At the same time, Zr and Ti are very immobile under near-atmospheric conditions, so they can be used as a conservative element to indicate the degree of weathering (Railsback, 2003; Yau *et al*., 1987). In addition to S isotope data, halloysite samples from various deposits follow an almost linear Zr *vs*. TiO_2 trend and strongly suggest a hypogene origin when compared to the Peruvian kaolins (Fig. 9). However, the possibility of the two elements behaving similarly during the hydrothermal alteration should be considered due to the almost linear trend.

Formation of halloysite

During stage 1 (Fig. 10a,b), halloysite formed due to the activity of S-rich geothermal waters of hypogene origin passing through the fault zone. Al, Fe, Mn and Ti, but not Si, were dissolved from andesitic tuffs (16−17 wt.% Al_2O_3) under acidic (pH <3) conditions. They then accumulated as Al hydroxides and formed halloysitic clay. The Na, K and Ca had already leached away from the clay body through the drainage system. Halloysitic clay accumulated (pH >4) among large limestone blocks which had fallen into the volcanic tuffs prior to mineralization. The base of the Kocadere River covers the large limestone blocks of the Hodul Unit, which also extends underneath the halloysite deposit. Iron and Mn were transported downwards and deposited due to increased pH as a thin crust of hematite and psilomelane on the surrounding surface of large limestone blocks within the halloysite body. The large limestone blocks within the clay body and the underlying limestone platform neutralized the pH of the geothermal waters, which rose up from the fault zone and flushed over the tuffs, as indicated by gypsum and anhydrite mineralization on the surface or in filled fractures of the limestone blocks. During stage 2 (Fig. 10c), the halloysite was concentrated by continuous *in situ* leaching and desilicification and depotassification processes under very low pH conditions (<3), which resulted in the transportation of Si and Mn. This process would progress the mineralization of hydrated halloysite underneath the well developed karstic drainage system. These changes in the pH of circulating water affected

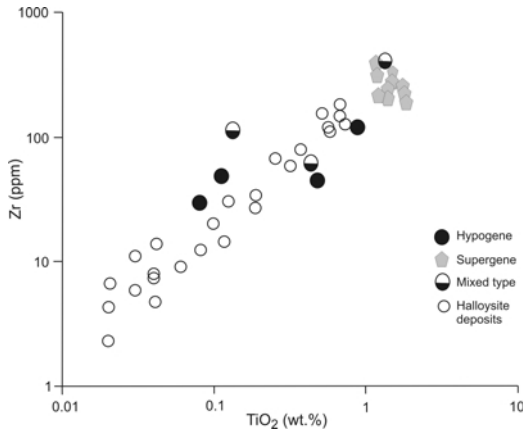

FIG. 9. Zr *vs*. TiO_2 plot of halloysite samples from the north and south mines (data are listed in Tables 2 and 3). Solid symbols represent hypogene, supergene and mixed-type origins of alunite and APS minerals from kaolin deposits in Peru (Dill *et al*., 1997).

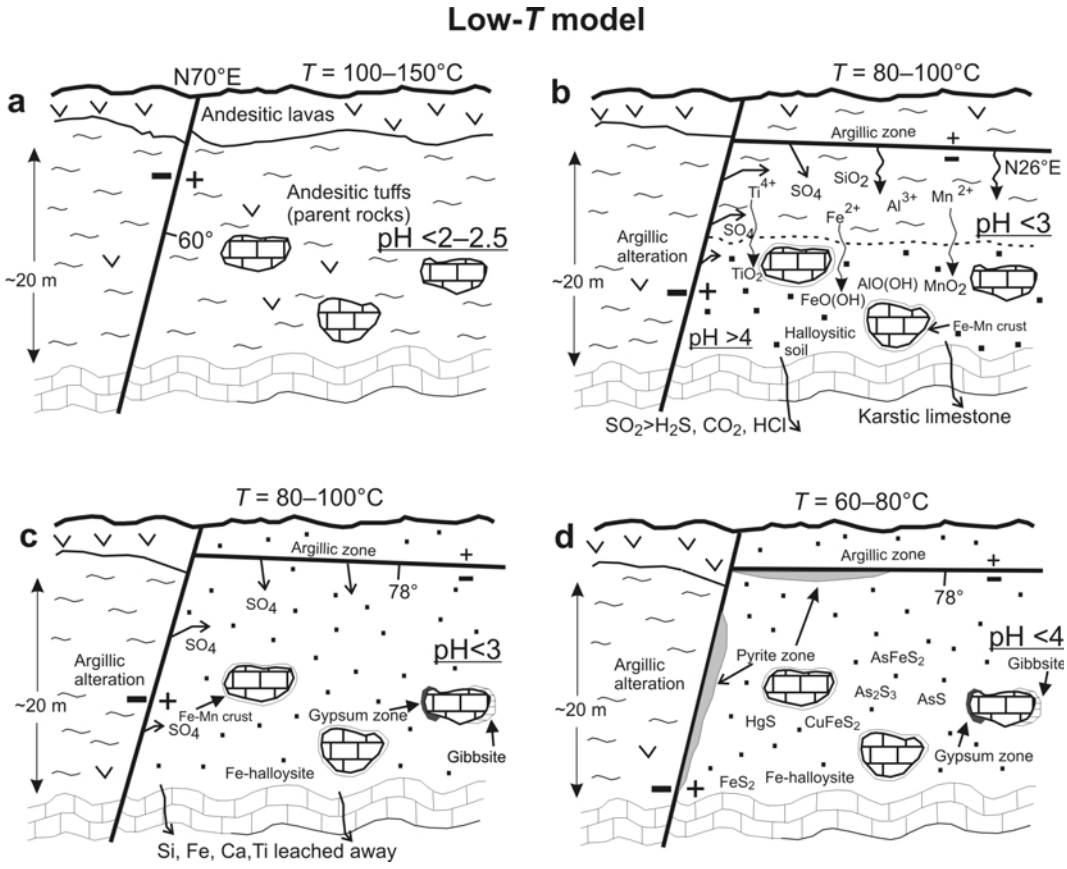

FIG. 10. A four-stage genetic model is proposed for the origin of the magmatic hydrothermal halloysite deposit. (a) Initial setting of andesitic tuffs as parent rock to the base karstic limestone. (b) Stage 1 involved geochemical leaching processes of andesitic tuffs and differential mobility of certain elements at different Eh/pH conditions. The fault clay was developed as an impermeable zone on the northern side of the halloysite quarry and halloysitization was enhanced to the south of the fault zone. The main wall-rock alteration stage of the magmatic hydrothermal system is responsible for the low sulphidization. (c) Stage 2 involved the ~50 wt.% reduction of the initial parent rocks to form halloysitic soil, *via* progressive downward Si-leaching, in the vertical direction, to depressions in the karstic limestone; upgrading halloysite through Si-leaching at pH = 2–3. (d) Stage 3 involved mainly pyrite mineralization along the fault zone and parent-rock/limestone contact and a very small amount of other sulphur minerals irregularly distributed within the halloysite body. No scale is used.

partial Si migration which resulted in the crystallization of halloysite from gel formed at a relatively low temperature (<100ºC). In the inorganic system, Si is more soluble than Al depending on pH, but in the organic system, in the presence of humic acids, Al is more soluble than Si (Huang & Keller, 1971). During stage 3 (Fig. 10d), sulphides formed mainly along the fault zones and other sulphur minerals (HgS, AsS, As_2S_3, $CuFeS_2$, $AsFeS_2$) precipitated irregularly within the clay body. Later, the environment was reducing, as indicated by pyrite mineralization, mostly along the fault and bottom zones to limestone (Öztürk *et al*., 2002).

During post-mineralization supergene activity, Fe, supplied by migration from the overlying altered andesitic rocks, infiltrated through the clay body and was deposited mainly around limestone blocks under high pH conditions. Goethite is irregularly distributed in the upper level of the clay body. Manganese was transported under low Eh conditions, but precipitated together with Fe around limestone blocks in a high-pH environment.

No pyrite, however, was found in the central part of the halloysite body. Gypsum is a true low-temperature hydrothermal product, which formed when sulphate-containing geothermal waters reacted with the surface of the limestone blocks. The oxygen content of circulating waters, fed by the fault zone, decreases with depth and consequently reducing conditions progressively increase towards the underlying limestone. Hence, pyrite-rich halloysite is found in this zone. Regardless of intense silica dissolution and migration, no silicification phenomena were observed in the vicinity of either clay quarry. It is probable that excess silica was precipitated far away from the clay deposits within the karstic environment.

The underlying carbonate rocks served not only to consume S-rich acidic geothermal waters, but also to infiltrate silica-rich leached-out solutions at pH <3 through the clay body. Consequently, through these geochemical leaching processes, ~50 wt.% reduction of the initial parent rocks should be expected in the field, as summarized below:

$$SiO_2\ (glass) + 2KAlSi_3O_8 + 2H^+ + 13H_2O = Al_2Si_2O_5(OH)_4.2H_2O + 2K^+ + 5H_4SiO_4$$

It is well documented that quartz precipitation is inhibited at low pH (Fournier, 1986). Hence it would have been transported in a gel form by rivers. At pH ~2, a large amount of Al transportation would be estimated. For instance, total dissolved Al increases with decreasing pH and as a result ~1,000 ppm Al dissolves at pH ~2 (Stoffregen, 1987). The acidity of the geothermal waters indicates an oxidizing medium and very low pH ($\leqslant 2$) conditions. A very small amount of alunite is also found close to limestone blocks in the Turplu halloysite quarry and these 3–5 cm specimens are used for K/Ar age determination of halloysite mineralization. No halloysite is observed in overlying, highly altered andesitic rocks, which are generally rich in smectite because the acidic solutions were exhausted before reaching the overlying country rocks. Andesitic tuffs were the parent rocks of the halloysite deposits. The upwards sequences of halloysite bodies, overlain by highly altered smectite-rich country rocks through a transitional zone containing decreasing amounts of halloysite, indicate possible consumption of H^+ ions in acidic geothermal solutions before reaching the surface rocks. With increasing alteration intensity from distal clay-dominated mineral assemblages to clay replacement cores, ~2–6 wt.% of some major oxides (MgO, CaO, Na_2O, K_2O) have been removed and these values increase for Al_2O_3 from 16 to >38 wt.% due to gibbsite formation.

Manganese has a high degree of mobility; it precipitates in the oxidation zone at high Eh and pH and remobilizes in the reducing zone at low Eh and pH conditions during the early stages of diagenesis. During chemical leaching processes, Mn is solubilized in acidic and reducing conditions and carried down the halloysitic clay profiles with the circulating waters (Frakes & Bolton, 1984, 1992). Aluminium and Ti mobilize under low Eh and pH conditions. Both Fe^{2+} and Fe^{3+} can be adsorbed on limestone blocks at higher pH values than Mn^{2+} (Stumm & Morgan, 1970), thus allowing greater removal of Fe than Mn from solution. As the result of these processes, Fe-Mn crusts, ~20–30 cm thick, are commonly observed surrounding some limestone blocks in the Turplu, Taban, Kızıldam and Kırıklar deposits. Our field observations of the Turplu deposits show similarities in the occurrences of alunite and hydrated halloysite, regardless of differences between percolating groundwater and hydrothermal models, in cave sediments from Belgium, France and the Guadalupe Mountains of New Mexico, in terms of drainage systems underlying karstic environments and the SO_2-bearing thermal waters, indicating the importance of acidic waters for the formation of hydrated halloysite.

We proposed that H_2S-SO_2 rose from the deep fault zone to surface levels, where it encountered oxygenated groundwater at the water table with input from rivers. Sulphuric acid formed and dissolved andesitic tuffs much faster than the andesite lavas and in the late stages of alteration, reacted with large limestone blocks to produce thin gypsum crusts on the surface (Hill, 1990) and inside the upper 10–20 cm of micro fractures. Also, thin and discontinuous gibbsite crusts are found on the surface of large limestone blocks indicating that dissolved Al ions in acidic thermal waters reacted with $CaCO_3$ and the consequent pH change caused precipitation of excess Al as gibbsite. Gibbsite may also precipitate in local areas with more intense Si-leaching in the limestone-block environment.

$$H_2S + 2O_2 = HSO_4^- + H^+ \qquad (pH \leqslant 2)$$

$$SO_2 + H_2O + \tfrac{1}{2}O_2 = HSO_4^- + H^+$$

$$HSO_4^- + H^+ + 2H_2O + CaCO_3 = CaSO_4.2H_2O + HCO_3^- + H^+$$

$$(K,Na,Ca)AlSi_3O_8 + H^+ + 7H_2O = Al(OH)_3 + 3H_4SiO_4 + Na^+ + K^+ + Ca^{2+}$$

It is possible that lithological differences in volcanic rocks influenced the differences in leaching processes and that underlying carbonate rocks provided excellent drainage conditions. The ascending hydrothermal solutions circulated within the clay body and passed through different migration pathways. The permeability in overlying fine pores of andesitic rocks changed significantly, which affected the stagnant flow of geothermal waters and reduced element mobility. This increased salinity and alkalinity, favouring the formation of smectite rather than kaolinite or halloysite outside the halloysite body in highly altered andesitic lavas (Kadir & Karakaş, 2004). In contrast, the permeability of the andesitic tuffs, the parent rocks of halloysite, was relatively high due to the carbonate blocks within the developing clay body and associated plastic deformation, which created different migration pathways and resulted in reduced salinity and alkalinity. Consequently, the enrichment in Al yielded halloysite and alunite.

Formation of alunite

A large alunite-halloysite deposit occurs in the north Turplu deposit area surrounded by advanced argillic alteration of andesitic rocks. The total thickness of the alunite deposit varies from 8 to 13 m. The alunite-halloysite mineralization has a shallow and open funnel-shaped morphology. Within the open quarry, two zones may be distinguished, although these zones are deformed and mixed due to the plastic nature of clay deposits, caused by recent tectonic movements. The first consists of a zone of halloysite ± kaolinite, which occurs only in the upper level grading outwards into a zone of smectite-illite-abundant argillic rocks. The second consists of variable amounts of alunite and very small amounts of kaolinite, Fe oxides and hydroxides. These two zones have irregular shape, where, in many places, they are intermixed and irregularly ditributed due to plastic deformation of the clay bodies.

The distribution and morphology of the alteration zones display the influence of acidic, sulphate-rich hypogene solutions and mobility limits of silica and sulphate ions on the occurrence of gibbsite and alunite. The alunite samples are compact and relatively hard with a white to pinkish colour; hardness tends to increase with the purity of alunite. Similar to the observations made in the halloysite deposit, large limestone blocks are surrounded by thin hematite and psilomelane crusts. The formation of alunite began simultaneously with the formation of gibbsite, but continued in strongly oxidizing environments at low pH with changing SO_4^{2-} contents. During stage 1 of alunite formation (Fig. 11a,b), Al, Fe, Ti, Ca, Mn, Na and K, but not Si, were dissolved from the initial parent rocks under acidic pH conditions with continuous intensive leaching as geothermal waters rose from the fault zone and infiltrated downwards in the karstic limestone drainage environment. As a result of acidic leaching processes, siliceous materials mostly accumulated in the upper level and resulted in the buildup of gibbsitic soil in the middle-lower level, with Fe and Ti oxides transported to the limestone.

During stage 2 (Fig. 11c), continuous decreases in pH (~2) levels of geothermal waters, possibly due to changes in sulphur sources and consequently, changes in their migration pathways, siliceous materials migrated by *in situ* leaching and desilicification through the karstic drainage system. As a result of Si migration and Al enrichment at low pH, gibbsite-rich clay zones were developed and, as a result, the bulk alunite samples are free of quartz. It is considered that the excess SiO_2, which was dissolved from andesitic tuffs, is used in the replacement of alunite by kaolinite (Stoffregen, 1987; Inoue & Utada, 1991a). However, this is a temperature-, Si content- and pH-dependent-reaction. If the temperature and Si concentration are very low, as in this case, halloysite precipitation should be expected, as observed in the upper level of the alunite quarry.

$$2(K,Na)Al_3(SO_4)_2(OH)_6 + 6H_4SiO_4 = 3Al_2Si_2O_5(OH)_4.2H_2O + 2(K^+,Na^+) + 4HSO_4^- + 7H_2O + 2H^+$$

Inoue & Utada (1991a) suggested that this reaction indicates that a solution with a lower pH favors precipitation of alunite, whereas alunite reacts with quartz to form dickite instead of halloysite, in higher-pH solutions at a depth of ~200 m in the Kamikita geothermal area, Japan. Furthermore, the pH fluctuation in the solution probably governed the average K^+ content of alunite; with more K^+ found at lower pH values.

During stage 3 (Fig. 11d), the widespread formation of alunite, which shows no clear boundary with halloysite or gibbsite, occurred in the zone of oxidation due to the influence of hypogene oxygenated circulating waters which led to the

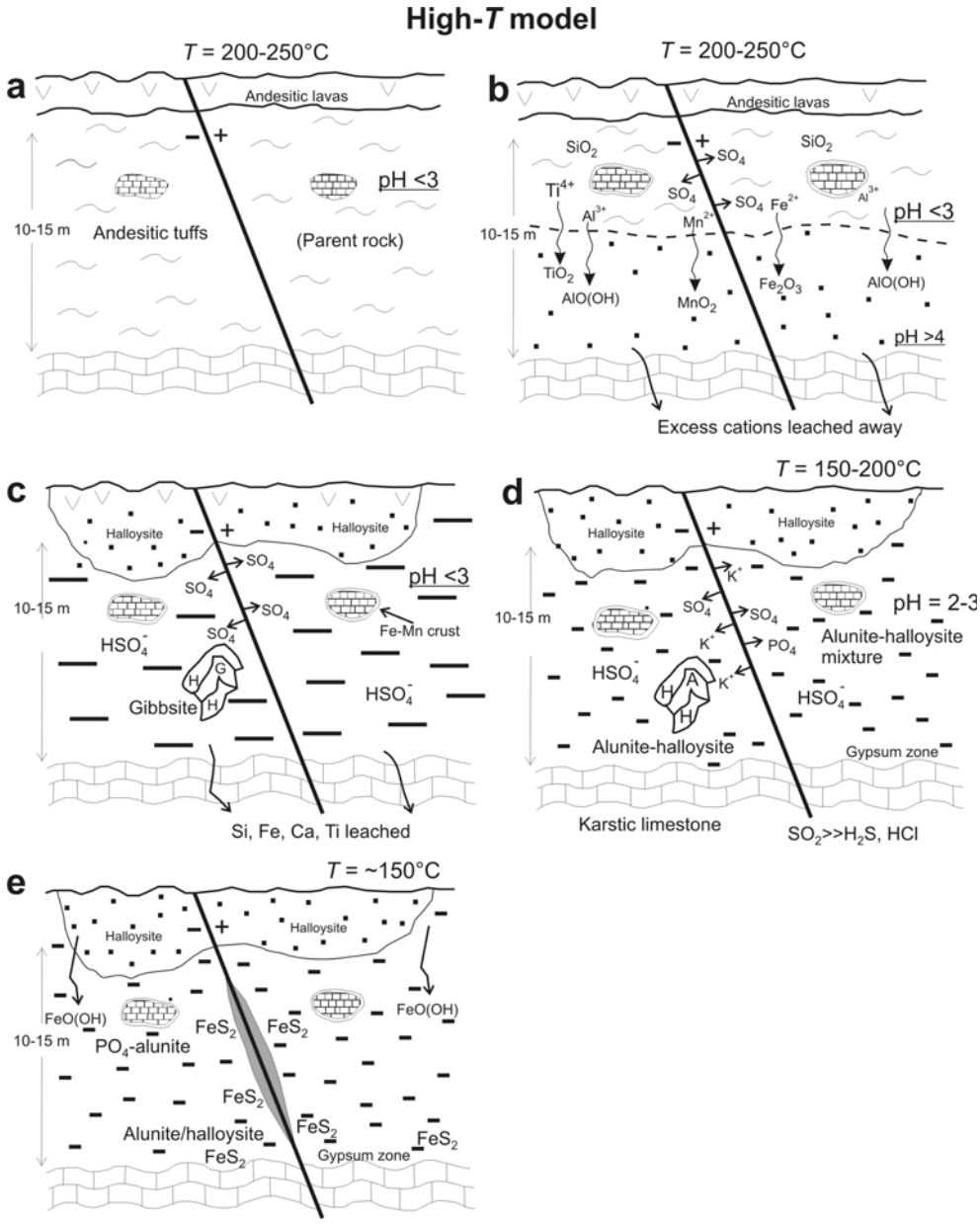

FIG. 11. Five-stage genetic model proposed for the origin of the magmatic hydrothermal alunite deposit. (a) Initial setting of andesitic tuffs as parent rock to the base karstic limestone. (b) Stage 1 involved geochemical leaching processes of andesitic tuffs and differential mobility of certain elements at different Eh/pH conditions. Both sides of the fault zone were affected by SO_4-rich hydrothermal solutions. (c) Stage 2 involved ~50 wt.% mass reduction of the initial parent rocks to form gibbsitic soil *via* progressive vertically downwards Si-leaching, to depressions in the karstic limestone; hence upgrading the gibbsite through Si leaching at pH <2. (d) Stage 3 involved alunitization from the intermediate parent rock of gibbsite with high-temperature kaolin group minerals nacrite and dickite detected. Some alunite samples are rich in phosphate. Gibbsite is found randomly between limestone blocks and halloysite. (e) Stage 4 involved mainly pyrite mineralization along the fault zone and the bottom zone to the consolidated limestone. Gypsum zones on the surface of limestone blocks are a common feature as supergene oxidation caused Fe-migration during the latest diagenetic stage. No scale is used.

initiation of further alteration. Hence, alunite was formed due to the presence of gibbsitic clays and input of HSO_4^-, transported through the fault zone. During stage 4 (Fig. 11e), the sulphide zones formed throughout the clay body by reduction of sulphate-rich geothermal waters and from Fe supplied by the alteration of overlying Fe-containing volcanic rocks. Pyrite formed during the later stages of hydrothermal activity and was widely distributed especially in the bottom zones. Fe hydroxide-pyrite enrichments in the fault zone and lower horizons show changes in redox conditions due to the presence of high-temperature bacterial degradation. In the latest stages, pyrite oxidation due to the influence of supergene meteoric waters is observed in the open quarries (Stoffregen, 1987). The schematic reactions for the formation of alunite are summarized below:

$$4SO_2 + 4H_2O = 3HSO_4^- + H_2S + 3H^+$$
$$3Al(OH)_3 + K^+ + H^+ + 2HSO_4^- = KAl_3(SO_4)_2(OH)_6 + 3H_2O \quad (pH \approx 2)$$

or,

$$3Al(OH)_3 + K^+ + 2H_2SO_4 = KAl_3(SO_4)_2(OH)_6 + 3H_2O + H^+ \quad (pH = 2-3)$$
$$3Al_2Si_2O_5(OH)_4 2H_2O + 2K^+ + 4HSO_4^- + 10H_2O = 2KAl_3(SO_4)_2 6H_2O + 6H_4SiO_4 + \tfrac{1}{2}O_2^{2-}$$

Latest-stage supergene alterations are as follows:

$$4FeS_2 + 4H_2O + 7H^+ = 4Fe^{2+} + HSO_4^- + 7H_2S_{(aq)} \quad \text{(Stoffregen, 1987)}$$
$$2FeS_2 + 7.5O_2 + 4H_2O = Fe_2O_3 + 4H^+ + 4HSO_4^-$$
$$2FeS_2 + 7.5O_2 + 5H_2O = 2FeO(OH) + 4HSO_4^- + 4H^+$$

The occurrence of H_2SO_4 in hydrothermal systems enhances the acidity of geothermal waters, provoking advanced argillic alteration zones (Ece & Schroeder, 2007). Acid-produced minerals typically comprise the following zones; kaolinite (up to 120ºC) and kaolinite plus dickite (120–180ºC), whereas alunite forms with a pH between 2.5 and 3.0 (Browne, 1998). Steam and oxidation of the ascending H_2S produced acid conditions favourable to the formation of alunite, halloysite and kaolinite, depending on the presence of partially Si-leached minerals and thin and discontinuous bauxitic clays partially surrounding limestone blocks, on the acidity levels and on the temperature of circulating waters in the alteration zone. *In situ* silica leaching is controlled by the acidity of ascending fluids.

The most common source of K^+ in alunite is the deep leaching of biotite- and hornblende-rich volcanic rocks (Browne, 1998). This process is supported in the Turplu alunite-halloysite deposits because all granodiorite exposures are biotite-rich in the Yenice-Gönen-Balya area and K-feldspar-rich granites occur in Danışment. Experimental evidence suggests that the fluid pH in the alunite zone was between 3 and 4 in the Matsukawa geothermal field, Japan (Browne, 1998). It is also estimated to range from 2 to 4 at 200–300ºC and have an appropriate dissolved sulphur content at Kamikita geothermal field, Japan (Inoue & Utada, 1991b). However, the pH of present-day sulphate-rich geothermal waters in the area of the Philippines ranges from 2.2 to 2.9 (SO_4^{2-} content 338–1288 mg/kg and temperature interval 25–99ºC) and in contrast, volcanic gas condensate waters have pH 1.0–2.0 (Nicholson, 1993). The ascending sulphate-rich geothermal waters may also be unusually acidic with pH 0–2; however, wall rock-water neutralization reactions at near-surface conditions can increase the pH. Acid-sulphate waters are defined as invariably superficial fluids formed by the condensation of geothermal gases into near-surface, oxygenated groundwater (Nicholson, 1993). The Turplu halloysite deposit is located at topographic levels partly below the water table due to the presence of the Kocadere River and hence fits with the above geological model.

The source of sulphur and fine-grained pyrite formation

The geographical setting and age difference between the igneous activity and mineralization of all halloysite deposits and Tertiary tectonic activity in the Balya-Yenice-Gönen area suggest that the sulphur may have been derived directly from the deep magmatic fluid or through dissolution and leaching of pre-existing sulphide-bearing magmatic sources (Ohmoto & Rye, 1979). At a later stage, it migrated through deep fracture systems as steam-heated SO_2-rich fluids. Due to the presence of numerous Cu-Zn-Pb-Ag deposits in the vicinity of the Yenice and Balya areas (Örgün *et al*., 2005), the small amount of sulphur in the volcanic rocks in the study area and the positive $\delta^{34}S$ values, we suggest that the limited solubility of sulphur in intermediate magmas was potentially responsible for the formation of magmatic sulphides and therefore, a deep magmatic fluid is the most likely source of the sulphur, and the leaching process is probably not universal. Field studies revealed that most shallow-

level granodiorites responsible for the sulphide mineralization are concentrated in the vicinity of the study area. Örgün *et al*. (2005) also suggested that the source of ore solutions was ~1000 m deep, based on fluid inclusion studies, which were exposed to surface levels in three different episodes. Sulphur contents of the peraluminous South Mountain batholith, Nova Scotia, Canada (Poulson *et al*., 1991), range from 6 to 570 ppm, with the granites (~20 ppm) having smaller sulphur contents than the grano-diorites (~300 ppm). Poulson *et al*. (1991) also reported that ~30–60% of the sulphur in the granodiorites (South Mountain, Nova Scotia) is present as pyrrhotite (a later phase), with most of the remainder present as sulphur substituted into biotite (an early phase). By this approach, it is more likely that the source of sulphur for the formation of skarn-type Pb-Zn-Cu sulphur deposits in the Yenice-Balya areas was by deep leaching of biotite-rich granodiorite intrusions.

The variation of $\delta^{34}S$ values of sulphide minerals and fluids depends on variations in temperature, redox conditions, pH and the isotope value of the source of the sulphur (Ohmoto, 1972). The geothermal waters probably had a large f_{O_2} due to the presence of alunite. The dominant sulphur species was H_2S, which originated from a deep source and $\delta^{34}S_{H_2S} \approx \delta^{34}S_{\text{sulphide mineral}}$ at temperature intervals >200ºC (Ohmoto & Goldhaber, 1997). Ohmoto & Rye (1979) suggested that the sulphur in the sulphates cannot be formed from primary sulphides by weathering. Volcanic rocks usually do not have enough permeability to allow deep circulation of surface waters. Therefore, hypogene fluids containing magmatic sulphur played an important role in the area studied. Pyrite and alunite are texturally and mineralogically distinct and alunite has larger $\delta^{34}S$ values than the pyrite, because although they have a similar origin, pyrite formed at a later stage. This precludes the use of the pyrite-alunite association as an indicator of a hypogene origin for alunite in the Turplu deposits.

Fine-grained pyrite within fault clays in the south Turplu halloysite deposit can be considered to result from a mixture of waters of hypogene origin and low-grade bacterial reduction of sulphate, due to its fine grain-size, spherical shape and the zoned nature of some pyrite grains. The slightly reduced $\delta^{34}S$ values of pyrite formation compared to alunite samples suggest a minor influence of sulphur-bearing bacteria at the closure stage of the hydrothermal activity (Table 5).

Alunite-halloysite environments include the steam-heated advanced argillic alteration zone and magmatic-hydrothermal replacement deposits. The oxidation of hydrogen sulphide to sulphate ions produces a minimum pH of ~2.8 ($H_2S_{(g)} + 2O_2 = 2H^+_{(aq)} + SO^{2-}_{4\,(aq)}$; at <400ºC). If waters are significantly more acidic than this pH value, a magmatic gas contribution should be taken into consideration (Nicholson, 1993). The magmatic hydrothermal environment led to a significant amount of magmatic heat and vapours ($4SO_2 + 4H_2O = 3H_2SO_4 + H_2S$) mixing with magmatic waters as the primary hypogene process (Rye *et al*., 1992), with a possible minor contribution of surface waters. This would explain why the advanced argillic alteration is found near to the surface in conditions where pressure is reduced and waters flush through the permeable tuffs. This model matches the Turplu deposits because the Kocadere River flows next to both areas (assuming that today's topography is similar to that during the Quaternary, based on hydrogeological studies (Yalçın, 1997) and/or the fact that there was abundant surface water ~0.7 Ma ago), and as a result the groundwater table is very close to surface mine-side. Hypogene alunites have slightly more enriched S isotopes than coexisting pyrite and gypsum in Turplu samples (Table 5). The small differences between the alunite and pyrite values may be a consequence of rapid isotopic exchange and relatively weak fractionation between the aqueous sulphides and sulphate species at moderate to high temperatures, particularly in acidic environments (Ohmoto Lasaga, 1982). An increase in f_{O_2} of the hydrothermal waters would result in a decrease in $\delta^{34}S$ of sulphides. Decreasing f_{O_2} would change the SO_2/H_2S ratio of the fluid towards H_2S dominance, so that the $\delta^{34}S$ of sulphides would increase to approximate the bulk S value.

Spatial and temporal relations of hydrothermal events

Acid-sulphate-type alunite-halloysite deposits appear to be spatially and temporally related to the shallow hydrothermal alteration of volcanic environments. These hydrothermally altered environments, which occur along faults, form small mineralized areas, suggesting greater permeability of the tuffs compared to the overlying lavas. The K-Ar ages of the various rock types are listed in Table 1. Based on

the K-Ar age dating of whole-rock, biotite and K-feldspar from granodiorites and andesites, the temporal relation of the hydrothermal episodes of mineralization in the Turplu area is summarized in Fig. 12. The calc-alkaline volcanism was active during the early Miocene and the volcanic succession displays repetitive sequences of agglomerate-lahars-tuffs-lavas, which were the final deposited materials. The intrusion of granodiorite through volcanic rocks caused tectonic uplift in the Balya complex in the vicinity of the volcanic rock–Permian limestone contact zone. The K-Ar data presented in Table 1 are consistent with other evidence that clearly shows the calc-alkaline volcanics and granodiorite intrusions of hybrid origin, formed from a similar source, interfinger during the early Miocene. The volcanics and the shallow-level epizonal granodioritic plutons are similar in geochemical character and in K-Ar age values, suggesting a common magma source. Magmatic activity shows close relationships spatially and temporally, as commonly observed in many volcanically active areas in Western Turkey (Altunkaynak & Yılmaz, 1998, 1999; Yılmaz *et al*., 2001). The calc-alkaline magmatic activity waned during the mid-Miocene, although during the Upper Miocene, widely distributed skarn-type Pb-Zn-Cu mineralization occurred in many areas of the Biga Peninsula (Örgün *et al*., 2005). These metallic

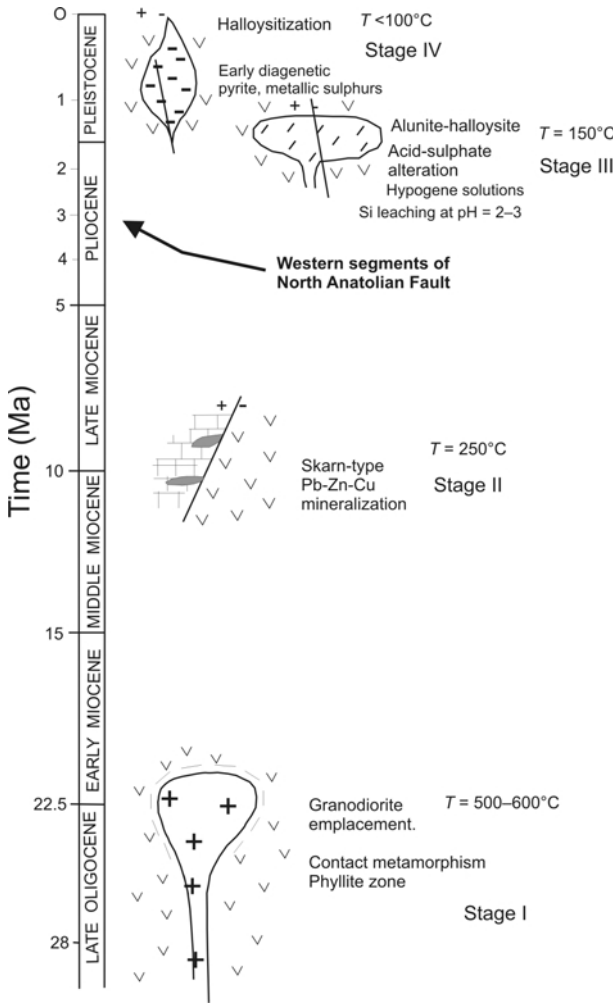

FIG. 12. Temporal illustration of hydrothermal stages through epochs in the Balya-Yenice-Gönen region. Modified from Inoue & Utada (1991b). No scale is used for the diagrams.

sulphur mineralizations, the biggest in Turkey, are the products of early-stage hydrothermal events after regional tectonic uplifts. The best exposures of the granodiorite-volcanic contact zones are seen to the north of Yenice. The contact metamorphic zone comprises mostly fine-grained phyllitic mudstones and tuffaceous rocks around its periphery.

At present, there are 27 hot springs in the Biga Peninsula with discharge temperatures of 31–104ºC and reservoir temperatures of 65–155ºC (Table 7). Eighteen are Na,SO_4-rich; two (Kestanbol and Tuzla) are Na,Cl-rich; and the rest are Na,Ca,Cl,HCO_3-rich. The closest hot spring to the Turplu deposit is Şamlı (~15 km northeast of the Turplu quarry). It has Na,Cl,SO_4-rich waters, a discharge temperature of 60ºC and a reservoir temperature of 108ºC (Yalçın & Sarp, 2008). The Gönen thermal waters have a discharge temperature of 70ºC, a reservoir temperature of up to 147ºC and contain Na,SO_4,HCO_3,Cl-rich waters. The Gönen and Ekşidere thermal waters are meteoric in origin, but the isotopic composition indicates that they are ~10,000 y old (palaeowater) (Yalçın, 1997).

The age of the 1200 km long, currently active NAF zone is the subject of scientific debate, with inception ages ranging from the latest Miocene to Pleistocene (Barka, 1992; Alpar & Yaltırak, 2002; Şengör *et al*., 2005). All young hydrothermal activity had initiated after the occurrence of the western segments of NAF zone in NW Turkey and therefore fossil geothermal fields must have formed during or after the initiation of the NAF. Only the Turplu quarry contains alunite mineralization in the Biga Peninsula. K-Ar age values for alunite from the north Turplu quarry (Table 1) range between 0.66 and 0.77 Ma, which probably indicates that alunite formation occurred over a relatively short time period ~0.7 Ma ago. In contrast, alunite

TABLE 7. Chemical classification of hot springs and their calculated reservoir temperatures in the Biga Peninsula. All thermal waters have pH ≈ 7 (Yalçın & Sarp, 2004).

Hot spring ID	Location	Chemical formulae	Measured surface temperature (ºC)	Calculated reservoir temperature (ºC)
1	Kocabaşlar	$NaCaSO_4$	36.1	65–70
2	Kırkgeçit (Küçük havuz)	$NaSO_4$	53.1	102–106
3	Kırkgeçit (Büyük havuz)	$NaSO_4$	53.1	102–106
4	Çan	$NaCaSO_4$	48.5	73–88
5	Bardakçılar (Uzancık)	$NaSO_4$	50.3	106–115
6	Bardakçılar Küçük kaynak	$NaSO_4$	58.9	106–115
7	Bardakçılar Yosunlu su	$NaSO_4$	48.9	106
8	Çan Karaılıca (Tepeköy)	$NaSO_4$	50.2	75–91
12	Külcüler	$NaSO_4$	33.7	84–94
14–40	Hıdırlar (South Yenice)	$NaSO_4$	84.8–86.3	108–122
15	Hıdırlar (drilling, S. Yenice)	$NaSO_4$	64	115–118
16	Hıdırlar Uyuz (S. Yenice)	$NaSO_4$	56.4	118
17	Kum Ilıca (NE Yenice)	$NaCaSO_4Cl$	69	104–148
18	Gönen	$NaSO_4HCO_3Cl$	68.9	103–147
19	Manyas	$NaCaHCO_3$	48.5	85
20	Kepekler	$NaClHCO_3$	64.4	89–93
21	Şamlı	$NaClSO_4$	60	108
22	Küçükçetmi	$NaHCO_3$	41.6	97–103
23	Güre	$NaSO_4$	60	105–108
24–43	Derman	$NaSO_4$	57.8	96–104
33	Karaağaç (Uyuz)	$NaHCO_3$	30.6	85
35	Kestanbol (Aegean Sea)	NaCl	75.5	120
36	Tuzla (Aegean Sea)	NaCl	104.4	155
37	Yukarı Palamutova	$NaCaSO_4Cl$	37.3	75
38	Alibeyköy	$NaSO_4$	31.5	67
39	Hıdırlar Köyiçi	$NaCaSO_4HCO_3$	44.7	100
41	Ekşidere	$CaHCO_3$	41.4	76
42	Adramis	$NaCaSO_4$	42.5	81

samples from the south Turplu halloysite deposit have ages between 0.11 and 0.49 Ma. This time difference between the two deposits was expected, based on field studies. Approximately 1 Ma ago, during the formation of alunite, the S and SO_4^{2-} contents and reservoir temperatures of fossil geothermal waters in this region were much greater than today. The young tectonic activity of the NAF zone has had a profound effect on the hydrology of the associated geothermal systems. The sulphate- and chloride-rich waters, which ascend from depth but rarely reach the water table, found paths to the surface, perhaps many kilometres from their main upflow regimes. In addition, surface waters mixed with deep ascending steam and gases and produced multi-condensate layers that were located above the deeper alkali-chloride water (Browne, 1998). This acid condensate fluid may also flow laterally in the subsurface, discharging as acid hot springs, which played an important role in the Turplu area. The proposed genetic model for the occurrence of alunite, halloysite and Pb-Cu-Zn mineralizations in the Turplu fossil geothermal field is shown in Fig. 13. In this model of steam-heating, we suggest that alunite was formed in the upflow and halloysite in the outflow sectors of the same hydrothermal system, whereas the insignificant occurrence of Pb-Cu-Zn mineralization across the Kocadere River was the by-product of another older outflow system. Alunite formed by the gradual desiccation of boiling mud pools within the permeable tuff zone as the hydrothermal activity began to wane.

CONCLUSIONS

Halloysite forms in low-pH environments within low-temperature geothermal fields. For halloysite to form, acidic geothermal water, good permeability (e.g. soft volcanic tuffs) and karstic environments for drainage systems are required for the migration of Si and other necessary cations. However, a high-temperature occurrence of halloysites is also found in the northern Turplu deposit, which is supported by the co-existence of alunite. Volcanic tuffs undergo hydrothermal alteration relatively easily in nature because of their permeability and amorphous structure. Hence, the tuffs of the study

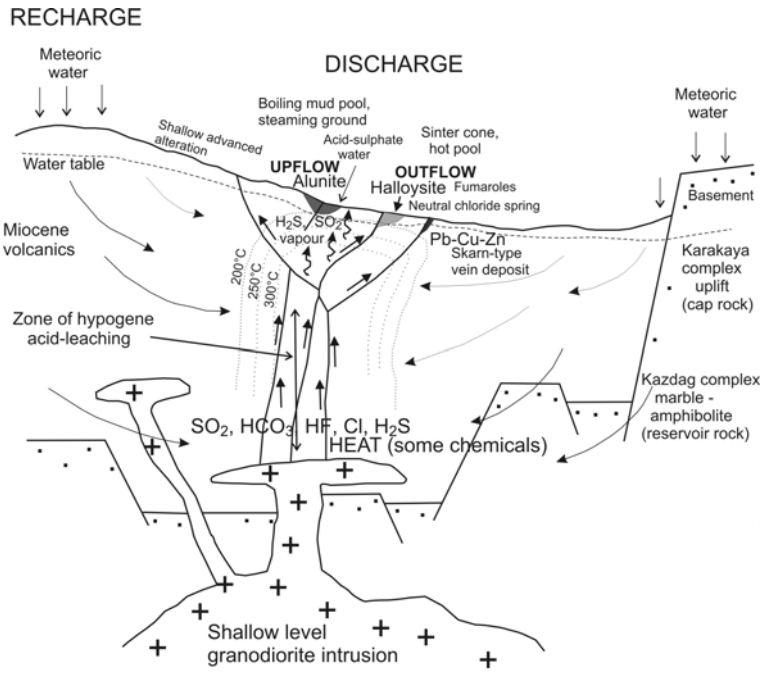

FIG. 13. Steam-heated genetic model for alunite and halloysite mineralization and acid-sulphate type alteration in the Turplu fossil geothermal field. The same model is valid for all other halloysite deposits. No scale is used. Modified from Heald *et al*. (1987) and Henley & Ellis (1983).

area were easily affected and transformed to clay minerals during the hydrothermal alteration.

Halloysite forms from andesitic tuffs and devitrified glasses by a dissolution-precipitation mechanism at low pH (2–3) in boiling-mud-pool environments. The changes of pH through time during hydrothermal activity strongly controlled the proposed dissolution-precipitation model. Gibbsite was the necessary intermediate parent mineral for the precipitation of alunite.

Miocene tectonism caused the uplift of giant carbonate blocks during the deposition of volcanic material. During the Pleistocene multi-stage leaching processes and under intense acidic conditions, Al-hydroxide gels converted to halloysite after crystallization prior to the ultimate removal of silica. The following criteria controlled the formation of halloysite: (1) the chemical composition and texture of andesitic tuffs as parent rocks; (2) the changes in pH of geothermal waters through time; (3) the amount and enrichment of dissolved acidic anions in geothermal waters; (4) the rate of the alteration reaction (this is very important as halloysite is a fast-forming meta-stable precursor to kaolinite); (5) all halloysite deposits are adjacent to the fault zone, which allowed the ascending geothermal waters to rise and flush over the parent tuffs, infiltrating downwards; (6) underlying or adjacent limestone blocks led to the formation of an excellent drainage system for leaching of undesirable cations; (7) the alunite deposit occurs in the upflow zone, where maximum SO_2 discharge was available along the fault zone, while all halloysite deposits occur in outflow zones where secondary SO_2 discharges were available; and (8) $\delta^{34}S$ values in alunite and pyrite samples indicate a hypogene origin of the sulphur source.

In addition to the above criteria, the changes in chemical composition of geothermal waters through time and the chemistry of the intermediate products in clay deposits also control the formation of alunite. The present study of halloysite mineralization indicates that similar hydrothermal events resulted from reactions of andesitic tuffs with different types of magmatic-hydrothermal solutions ascending through different discharge veins. The main geothermal activity and acid-sulphate alterations for the mineralizations of alunite and halloysite occurred after the onset of NAF-related faulting in the Biga Peninsula. The $\delta^{34}S$ values and P_2O_5 enrichment in alunite nodules suggest a deep magmatic source for the geothermal waters that passed through the shallow-level granodiorite intrusions.

ACKNOWLEDGMENTS

This research was made possible with the support of NSF-TÜBİTAK International Program YDABAG Project No: 101Y137 (Ö.I. Ece) and NSF Grant No. INT-0138023 (P.A. Schroeder). Additional financial support was obtained from the Istanbul Technical University Research Fund (Project No: 30345). We express our gratitude to Dr John P. Shields and Dr Mark A. Farmer of the Center for Ultrastructural Research for FE-SEM and HRTEM studies at The University of Georgia, Dr Douglas Crowe and Ms Julie Cox for $\delta^{34}S$ isotope studies at the University of Georgia and Dr Kurt Ferguson for the $\delta^{18}O$ and δD studies at Southern Methodist University. We also express our gratitude to Mustafa Bal and İlhami Tezcan of KALEMADEN Corp. and Yüceer Göver, Dr İhsan Bozdoğan and Ali Uygun of ESAN Eczacıbaşı Corp. for logistical support and accommodation during the field studies. We are especially grateful to Dr George Christidis of Crete Technical University, Greece, as well as Drs Aral Okay and Murat Budakoğlu of Istanbul Technical University, Turkey for their review comments, which significantly improved the organization and quality of this paper.

REFERENCES

Alpar B. & Yaltırak C. (2002) Characteristic features of the North Anatolian Fault in the Marmara region and its tectonic evolution. *Marine Geology*, **190**, 329–350.

Altunkaynak Ş. & Yılmaz Y. (1998) The Mount Kozak magmatic complex, Western Anatolia. *Journal of Volcanology and Geothermal Research*, **85**, 211–231.

Altunkaynak Ş. & Yılmaz Y. (1999) The Kozak Pluton and its emplacement. *Geological Journal*, **34**, 257–274.

Bailey S.W. (1989) Halloysite – A critical assessment. Pp. 89–98 in: *Proceedings of the 9th International Clay Conference; Strasbourg, France* (V.C. Farmer and T. Tardy, editors). Sciences Géologiques Mémoires (Strasbourg), **86**.

Barka A.A. (1992) The North Anatolian fault zone. *Annales Tectonicae*, **6**, 164–195.

Brimhall G.H.Jr. & Ghiorso M.S. (1983) Origin and ore-forming consequences of the advanced argillic alteration process in hypogene environments by magmatic gas contamination of meteoric fluids. *Economic Geology*, **78**, 73–90.

Browne P.R.L. (1998) *Hydrothermal Alteration*.

University of Auckland, Geothermal Institute, New Zealand, 70 pp.

Cornell R.M. & Schwertmann U. (1996) *The Iron Oxides: Structure, Properties, Reactions, Occurrences, and Uses*. Wiley-VCH, 573 pp.

Cunningham C.G., Rasmussen J.D., Steven T.A., Rye R.O., Rowley P.D., Romberger S.B. & Selverstone J. (1998) Hydrothermal uranium deposits containing molybdenum and fluorite in the Marysvale volcanic field, west-central Utah. *Mineralium Deposita*, **33**, 477–494.

Dill H.G. (2001) The geology of aluminium phosphates and sulphates of the alunite group minerals: a review. *Earth Science Reviews*, **53**, 35–93.

Dill H.G., Bosse H.R., Henning K.H., Fricke A. & Ahrendt H. (1997) Mineralogical and chemical variations in hypogene and supergene kaolin deposits in a mobile fold belt the Central Andes of northwestern Peru. *Mineralium Deposita*, **32**, 149–163.

Ece Ö.I. & Nakagawa Z. (2003) Alteration of volcanic rocks and genesis of kaolin deposits in Şile region, northern Istanbul, Turkey. Part II. Differential mobility of elements. *Clay Minerals*, **38**, 529–550.

Ece Ö.I. & Schroeder P.A. (2007) Clay mineralogy and chemistry of the halloysite and alunite deposits in the Turplu area, Balıkesir, Turkey. *Clays and Clay Minerals*, **55**, 18–36.

Elliott W.C., Edenfield A.M., Wampler J.M., Matisoff G. & Long P.E. (1999) The kinetics of the smectite to illite transformation in Cretaceous bentonites, Cerro Negro, New Mexico. *Clays and Clay Minerals*, **47**, 286–296.

Fournier R.O. (1986) The behavior of silica in hydrothermal solutions. Pp. 45–61 in: *Geology and Geochemistry of Epithermal Systems* (B.R. Berger & P.M. Bethke, editors). Reviews in Economic Geology, **2**. Society of Economic Geologists, El Paso, Texas, USA.

Frakes L. & Bolton B. (1984) Origin of manganese giants: Sea-level change and anoxic-oxic history. *Geology*, **12**, 83–86.

Frakes L. & Bolton B. (1992) Effects of ocean chemistry, sea level, and climate on the formation of primary sedimentary manganese ore deposits. *Economic Geology*, **87**, 1207–1217.

Fytikas M., Giuliani O., Innocenti F., Marinelli G. & Mazzuoli R. (1976) Geochronological data on recent magmatism of Aegean Sea. *Tectonophysics*, **31**, 29–34.

Fytikas M., Innocenti F., Manetti P., Mazzuoli R., Peccerillo A. & Villari L. (1984) Tertiary to Quaternary evolution of volcanism in the Aegean Region. Pp. 687–699 in: *The Geological Evolution of the Aegean Mediterranean* (J.E. Dixon & A.H.F. Robertson, editors). Special Publication **17**, The Geological Society, London.

Genç C.Ş. (1998) Evolution of the Bayramiç magmatic complex, northwestern Anatolia. *Journal of Volcanology and Geothermal Research*, **85**, 233–249.

Gözler Z. (1984) *Çannakkle Boğazı doğusu – Marmara Denizi güneyi – Bandırma-Balıkesir-Edremit ve Ege Denizi arasındaki alanın jeolojisi ve kompilasyonu*. MTA (Mineral Reseach and Exploration Institute) Open File Report **7430**.

Harris C., Compton J.S. & Bevington S.A. (1999) Oxygen and hydrogen isotope composition of kaolinite deposits, Cape Peninsula, South Africa; low-temperature, meteoric origin. *Economic Geology*, **94**, 1353–1366.

Harris N.B.W., Pearce J.A. & Tindle A.G. (1986) Geochemical characteristics of collision-zone magmatism. Pp. 67–81 in: *Collision Tectonics* (M.P. Coward & A.C. Ries, editors). Special Publication **19**. The Geological Society, London.

Harris N.B.W., Kelley S. & Okay A.I. (1994) Post-collision magmatism and tectonics in northwest Anatolia. *Contributions to Mineralogy and Petrology*, **117**, 241–252.

Harvey C.C. & Murray H.H. (1993) The geology, mineralogy and exploitation of halloysite clays of Northland, New Zealand. Pp. 233–248 in: *Kaolin Genesis and Utilization* (H. Murray, W. Bundy & C. Harvey, editors) CMS Special Publication, **1**.

Hayba D.O., Bethke P.M., Heald P. & Faley N.K. (1985) Geologic, mineralogic and geochemical characteristics of volcanic-hosted epithermal precious-metal deposits. *Reviews in Economic Geology*, **2**, 129–167.

Heald P., Foley N.K. & Hayba D.O. (1987) Comparative anatomy of volcanic-hosted epithermal deposits: acid-sulphate and adularia-sericite types. *Economic Geology*, **82**, 1–26.

Henley R.D. & Ellis A.J. (1983) Geothermal systems ancient and modern: a geochemical review. *Earth Science Reviews*, **19**, 1–50.

Herece E. (1990) 1953 Yenice-Gönen earthquake fracture and the extension of North Anatolian Fault zone in Biga peninsula. *Mineral Research and Exploration Bulletin*, **11**, 47–59.

Hill C.A. (1986) Fiume Vento cave, Italy – 'a baby' Carlsbad Cavern. *Cave Research Foundation Annual Report*, **28**, 18–20.

Hill C.A. (1987) Geology of Carlsbad Cavern and other caves in the Guadalupe Mountains, New Mexico and Texas. *New Mexico Bureau of Mines and Mineral Resources Bulletin*, **117**, 150.

Hill C.A. (1990) Sulfuric acid speleogenesis of Carlsbad cavern and its relationship to hydrocarbons, Delawarer basin, New Mexico and Texas. *American Association of Petroleum Geologists Bulletin*, **74**, 1685–1694.

Holland H.D. (1965) Some applications of thermochemical data to problems of ore deposits, II. Mineral

assemblages and the composition of ore-forming fluids. *Economic Geology*, **60**, 1101–1166.

Holland H.D. (1967) Gangue minerals in hydrothermal deposits. Pp. 382–436 in: *Geochemistry of Hydrothermal Ore Deposits* (H.L. Barnes, editor) New York, Holt, Rinehart and Winston.

Huang W.H. & Keller W.D. (1971) Dissolution of clay minerals in dilute organic acids at room temperature. *American Mineralogist*, **56**, 1082–1095.

Inoue A. & Utada M. (1991a) Hydrothermal alteration related to Kuroko mineralization in the Kamikita area, Northern Honshu, Japan, with special reference to the acid-sulfate alteration. *Geological Survey of Japan Report*, **277**, 39–48.

Inoue A. & Utada M. (1991b) Hydrothermal alteration in Kamikita Kuroko mineralization area, Northern Honshu, Japan. *Mining Geology*, **41**, 203–218.

Ishihara S., Jin M.S. & Sasaki A. (2000) Source diversity of ore sulfur from Mesozoic-Cenozoic mineral deposits in the Korean Peninsula region. *Resource Geology*, **50**, 203–212.

Jeong G.Y. (1998) Formation of vermicular kaolinite from halloysite aggregates in the weathering of plagioclase. *Clays and Clay Minerals*, **46**, 270–279.

Joussein E., Petit S., Churchman J., Theng B., Righi D. & Delvaux B. (2005) Halloysite clay minerals – A review. *Clay Minerals*, **40**, 383–426.

Kadir S. & Karakaş Z. (2004) Mineralogy, chemistry and origin of halloysite, kaolinite and smectite from Miocene ignimbrites, Konya, Turkey. *Neues Jahrbuch für Mineralogie-Abhandlungen*, **177**, 113–132.

Karacık Z. & Yılmaz Y. (1998) Geology of the ignimbrites and the associated volcano-plutonic complex of the Ezine area, northwestern Anatolia. *Journal of Volcanology and Geothermal Research*, **85**, 251–264.

Keller W.D. (1963) Hydrothermal kaolinitization (endellization) of volcanic glassy rock. *Clays and Clay Minerals*, 10th International Conference, pp. 333–343.

Keller W.D. & Hanson R.F. (1968) Hydrothermal alteration of a rhyolitic flow breccia near San Luis Potosi, Mexico, to refractory kaolin. *Clays and Clay Minerals*, **16**, 223–230.

Keller W.D. & Hanson R.F. (1969) Hydrothermal argillation of volcanic pipes in limestone in Mexico. *Clays and Clay Minerals*, **17**, 9–12.

Keller W.D., McGrain P., Reesman A.L. & Saum N.M. (1966) Observations on the origin of endellite in Kentucky and their extension to 'indianaite'. *Clays and Clay Minerals*, **3**, 97–120.

Keller W.D., Hanson R.F., Huang W.H. & Cervantes A. (1971) Sequential active alteration of rhyolitic volcanic rock to endellite and a precursor phase of it at a spring in Michoacan, Mexico. *Clays and Clay Minerals*, **19**, 121–127.

Kittrick J.A. (1969) Soil minerals in the Al_2O_3-SiO_2-H_2O system and a theory of their formation. *Clays and Clay Minerals*, **17**, 157–167.

Le Maitre R.W. (1989) *A Classification of Igneous Rocks and Glossary of Terms*. Blackwell Science, Oxford, 193 pp.

Love D.A., Clark A.H., Jay Hodson C., Mortensen I.K., Archibald D.A. & Farrar E. (1998) The timing of adularia-sericite-type mineralization and alunite-kaolinite-type alteration, Mount Skukum epithermal gold deposit, Yukon Territory, Canada: $^{40}Ar/^{39}Ar$ and U-Pb geochronology. *Economic Geology*, **93**, 437–462.

Murray H.H. & Keller W.D. (1993) Kaolins, kaolins, and kaolins. Pp. 1–25 in: *Kaolin Genesis and Utilization* (H. Murray, W. Bundy & C. Harvey, editors). Special Publication, **1**. The Clay Minerals Society, Boulder, Colorado, USA.

Nicholson K. (1993) *Geothermal Fluids; Chemistry and Exploration Techniques*. Springer-Verlag, Berlin, 262 pp.

Ohmoto H. (1972) Systematics of sulfur and carbon isotopes in hydrothermal ore deposits. *Economic Geology*, **67**, 551–579.

Ohmoto H. & Goldhaber M.B. (1997) Sulfur and carbon isotopes. Pp. 517–612 in: *Geochemistry of Hydrothermal Ore Deposits* 3rd edition (H.L. Barnes, editor). Wiley, New York.

Ohmoto H. & Lasaga A.C. (1982) Kinetics of reactions between aqueous sulfates and sulfides in hydrothermal systems. *Geochimica et Cosmochimica Acta*, **46**, 1727–1748.

Ohmoto H. & Rye R.O. (1979) Isotopes of sulfur and carbon. Pp. 509–567 in: *Geochemistry of Hydrothermal Ore Deposits* (H.L. Barnes, editor). New York, Holt, Rinehart and Winston.

Okay A.I., Siyako M. & Burkan K.A. (1991) Geology and tectonic evolution of the Biga Peninsula, northwest Turkey. *Bulletin of Istanbul Technical University*, **44**, 191–256.

Okay A.I., Demirbağ E., Kurt H., Okay N. & Kuşçu I. (1999) An active, deep marine strike-slip basin along the North Anatolian Fault in Turkey. *Tectonics*, **18**, 129–147.

Okay A.I., Kaşlılar-Özcan A., İmren C., Boztepe-Güney A., Demirbağ E. & Kuşçu I. (2000) Active faults and evolving strike-slip basins in the Marmara Sea, northwest Turkey: a multichannel seismic reflection study. *Tectonophysics*, **321**, 189–218.

Öngen S. (1978) Genetische aussagen uber das Çavuşlu–Karaköy granotoid massiv. *İstanbul Üniversity, Fen Fakultesi Mecmuasi*, **B43**, 141–150.

Örgün Y., Gültekin A.H. & Onal A. (2005) Geology, mineralogy and fluid inclusion data from the Arapucan Pb-Zn-Cu-Ag deposit, Çanakkale, Turkey. *Journal of Asian Earth Sciences*, **25**, 629–642.

Öztürk H., Hein J.R. & Hanılçı N. (2002) Genesis of the Doğankuzu and Mortaş bauxite deposits, Taurides, Turkey: Seperation of Al, Fe, and Mn and implications for passive margin metallogeny. *Economic Geology*, **97**, 1063–1077.

Pearce J.A., Bender J.F., De Long S.E., Kidd W.S.F., Low P.J., Güner Y., Saroglu F., Yılmaz Y., Moorbath S. & Mitchell J.J. (1990) Genesis of collision volcanism in eastern Anatolia, Turkey. *Journal of Volcanology and Geothermal Research*, **44**, 189–229.

Perruchot A., Dupuis C., Brouard E., Nicaise D. & Ertus R. (1997) L'halloysite karstique: comparaison des gisements types de Wallonie (Belgique) et du Perigord (France). *Clay Minerals*, **32**, 271–287.

Polyak V.J. & Güven N. (1996) Alunite, natroalunite and hydrated halloysite in Carlsbad Cavern and Lechuguilla cave, New Mexico. *Clays and Clay Minerals*, **44**, 843–850.

Poulson S.R., Kubilius W.P. & Ohmoto H. (1991) Geochemical behavior of sulfur in granitoids during intrusion of the South Mountain Batholith, Nova Scotia, Canada. *Geochimica et Cosmochimica Acta*, **55**, 3809–3830.

Railsback L.B. (2003) An earth scientist's periodic table of the elements and their ions. *Geology*, **31**, 737–740.

Rye R.O., Bethke P.M. & Wasserman W.D. (1992) The stable isotope geochemistry of acid sulfate alteration. *Economic Geology*, **87**, 225–262.

Sakai H. & Matsubaya O. (1977) Stable isotope studies of Japanese geothermal systems. *Geothermics*, **5**, 97–124.

Sengör A.M.C., Tüysüz O., Imren C., Sakinc M., Eyidogan H., Görür N., Le Pichon X. & Rangin C. (2005) The North Anatolian Fault: A new look. *Annual Review of Earth and Planetary Sciences*, **33**, 37–112.

Sheppard S.M.F. & Gilg H.A. (1996) Stable isotope geochemistry of clay minerals. *Clay Minerals*, **31**, 1–24.

Siyako M., Bürkan K.A. & Okay A.I. (1989) Tertiary geology and hydrocarbon potential of the Biga and Gelibolu Peninsulas. *Turkish Association of Petroleum Geologists Bulletin*, **1**, 183–199.

Stoffregen R. (1987) Genesis of acid-sulfate alteration and Au-Cu-Ag mineralization at Summitville, Colorado. *Economic Geology*, **82**, 1575–1591.

Stumm W. & Morgan J.J. (1970) *Aqueous Chemistry*. Wiley, New York, 583 pp.

Su C. & Harsh J.B. (1994) Gibbs free energies of formation at 298 K for imogolite and gibbsite from solubility measurements. *Geochimica et Cosmochimica Acta*, **58**, 1667–1677.

Sun S.S. & McDonough W.F. (1989) Chemical and isotopic systematics of oceanic basalts: implications for mantle composition and processes. Pp. 313–345 in: *Magmatism in the Ocean Basins* (A.D. Saunders & M.J. Norry, editors). Special Publication, **42**. The Geological Society, London.

Tazaki K. (2005) Microbial formation of a halloysite-like mineral. *Clays and Clay Minerals*, **53**, 224–233.

Thorpe R.S., Francis P.W. & O'Callaghan L. (1984) Relative roles of source composition, fractional crystallization and crustal contamination in the petrogenesis of Andean volcanic rocks. *Philosophical Transactions of the Royal Society London*, **A310**, 675–692.

Uygun A. (1999) KB Anadolu'da karbonat kayaçların içine yerleşmiş bazı halloysit yataklarının jeolojisi ve oluşumu. (Occurrence and geology of some halloysite deposits embedded in carbonate rocks in NW Anatolia). *MTA Dergisig*, **121**, 141–151.

Whitney J.A. (1984) Fugacities of sulfurous gases in pyrrhotite-bearing silicic magmas. *American Mineralogist*, **69**, 69–78.

Winchester J.A. & Floyd P.A. (1977) Geochemical discrimination of different magma series and their differentiation products using immobile elements. *Chemical Geology*, **20**, 325–343.

Yalçın T.H. (1997) Hydrogeological investigation of Gönen and Ekşidere (Balıkesir) thermal waters (NW Turkey). Pp. 275–300 in: *Active Tectonics of Northwestern Anatolia – The Marmara Poly-Project* (C. Schindler & M. Pfister, editors), Hochschulverlag AG an der ETH Zürich.

Yalçın T.H. & Sarp S. (2008) *Investigation of thermal waters in Biga Peninsula*. Mineral Research and Exploration (MTA) open-file report (in prep).

Yau Y.C., Peacor D.R. & Essene E.J. (1987) Hydrothermal treatment of smectite, illite and basalt to 460ºC – comparison of natural with hydrothermally formed clay minerals. *Clays and Clay Minerals*, **35**, 241–250.

Yılmaz Y., Genç Ş.C., Karacık Z. & Altunkaynak Ş. (2001) Two contrasting magmatic associations of NW Anatolia and their tectonic significance. *Journal of Geodynamics*, **31**, 243–271.

Ziegler K., Hsieh J.C.C., Chadwick O.A., Kelly E.F., Hendricks D.M. & Savin S.M. (2003) Halloysite as a kinetically controlled end product of arid-zone basalt weathering. *Chemical Geology*, **202**, 461–478.